Journal of the Mechanics and Physics of Solids 61 (2013) 2331–2359

Contents lists available at ScienceDirect

Journal of the Mechanics and Physics of Solids

journal homepage: www.elsevier.com/locate/jmps

Adiabatic shear banding and scaling laws in chip formation with application to cutting of Ti–6Al–4V

A. Molinari [a,b,*], X. Soldani [b], M.H. Miguélez [b]

[a] Laboratoire d'Etude des Microstructures et de Mécanique des Matériaux, LEM3, UMR CNRS 7239, Labex Damas, Université de Lorraine, Ile du Saulcy, 57045 Metz Cedex, France

[b] Department of Mechanical Engineering, Universidad Carlos III de Madrid, Avda. Universidad 30, 28911 Leganés, Madrid, Spain

ARTICLE INFO

Article history:
Received 6 March 2013
Accepted 28 May 2013
Available online 12 June 2013

Keywords:
Adiabatic shear banding
Metal cutting
Numerical and analytical modeling
Scaling laws
Convective effects

ABSTRACT

The phenomenon of adiabatic shear banding is analyzed theoretically in the context of metal cutting. The mechanisms of material weakening that are accounted for are (i) thermal softening and (ii) material failure related to a critical value of the accumulated plastic strain. Orthogonal cutting is viewed as a unique configuration where adiabatic shear bands can be experimentally produced under well controlled loading conditions by individually tuning the cutting speed, the feed (uncut chip thickness) and the tool geometry. The role of cutting conditions on adiabatic shear banding and chip serration is investigated by combining finite element calculations and analytical modeling. This leads to the characterization and classification of different regimes of shear banding and the determination of scaling laws which involve dimensionless parameters representative of thermal and inertia effects. The analysis gives new insights into the physical aspects of plastic flow instability in chip formation. The originality with respect to classical works on adiabatic shear banding stems from the various facets of cutting conditions that influence shear banding and from the specific role exercised by convective flow on the evolution of shear bands. Shear bands are generated at the tool tip and propagate towards the chip free surface. They grow within the chip formation region while being convected away by chip flow. It is shown that important changes in the mechanism of shear banding take place when the characteristic time of shear band propagation becomes equal to a characteristic convection time. Application to Ti–6Al–4V titanium are considered and theoretical predictions are compared to available experimental data in a wide range of cutting speeds and feeds. The fundamental knowledge developed in this work is thought to be useful not only for the understanding of metal cutting processes but also, by analogy, to similar problems where convective flow is also interfering with adiabatic shear banding as in impact mechanics and perforation processes. In that perspective, cutting speeds higher than those usually encountered in machining operations have been also explored.

1. Introduction

Adiabatic shear bands (ASB) are narrow zones with thickness of the order of few micro-meters where shear deformation is highly localized (Rogers, 1979; Bai and Dodd, 1992; Wright, 2002). They are observed in metals subject to fast deformation processes and are generally the result of thermal softening due to heating by plastic deformation (Tresca, 1878; Zener and

* Corresponding author at: Laboratoire d'Etude des Microstructures et de Mécanique des Matériaux, LEM3, Labex Damas, Université de Lorraine, Ile du Saulcy, 57045 Metz Cedex, France. Tel.: +33 3 87 31 53 69; fax: +33 3 87 31 53 66.
E-mail address: alain.molinari@univ-lorraine.fr (A. Molinari).

0022-5096/$ - see front matter © 2013 Elsevier Ltd. All rights reserved.
http://dx.doi.org/10.1016/j.jmps.2013.05.006

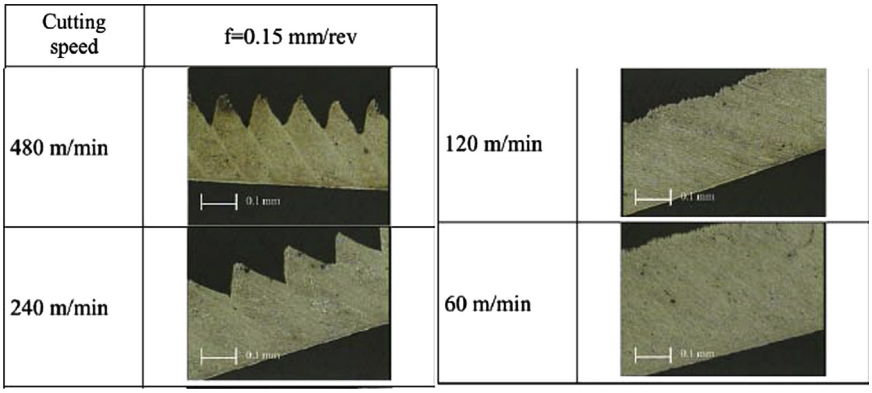

Fig. 1. Chip morphology in orthogonal cutting of 42CrMo4 steel (AFNOR: 42CD4) with a rake angle of −3°, according to Moufki et al. (2004). A transition from continuous chip to segmented chip is observed with increasing of the cutting speed. At high cutting speed the chip segments are delimited by adiabatic shear bands where plastic flow is localized.

Hollomon, 1944). ASB are associated to peaks of temperature which coincide with strain localization zones. Temperature peaks can happen in fast processes since in this case heat conduction has no enough time to smooth the temperature field.

At high strain rates, shear banding is frequently a consequence of thermal softening, but at lower rates shear bands can be generated (or at least influenced) by other softening mechanisms (decay of the stress carrying capacity) due to dynamic recrystallisation (Rittel et al, 2008) phase transformation or material damage (Cox and Low, 1974); Dodd and Atkins, 1983.

Adiabatic shearing was investigated in split torsional Hopkinson bars by Marchand and Duffy (1988). Modeling was performed with linearized stability analyses (Clifton, 1980; Bai, 1982; Molinari, 1985) non-linear analytical approaches (Molinari and Clifton, 1983, 1987; Wright, 1990, 1994; Mercier and Molinari, 1998) and numerical simulations using finite difference and finite element approaches (Batra and Ravinsankar, 2000; Bonnet-Lebouvier et al., 2002; Meyers and Kuriyama, 1986; Wright and Batra, 1985; Wright and Walter, 1987; Zhou et al., 1996b). A comprehensive modeling of adiabatic shearing has been established including the analysis of the onset, growth, interaction and propagation of adiabatic shear bands and the role of material parameters and loading conditions. Reviews on ASB can be found in Bai and Dodd (1992) and Wright (2002).

Orthogonal cutting is a quite interesting process for analyzing adiabatic shear banding. Fig. 1 shows chip serration due to adiabatic shearing during orthogonal cutting of 42CrMo4 steel (Moufki et al., 2004). At high cutting speeds a family of adiabatic shear bands with regular spacing is observed in the chip. Each chip serration is associated to a well formed macroscopic shear band.

The process of orthogonal cutting is unique by offering the possibility of generating ASB under well controlled conditions by tuning individually several control parameters: cutting speed, feed (uncut chip thickness), and tool geometry (inclination of the tool rake face and tool edge radius). There exist just few other experimental configurations where ASB can be produced under well controlled conditions. Shear banding can be triggered in a thin tube subject to rapid torsion on split torsional Hopkinson bars (Marchand and Duffy, 1988). In this experiment a single adiabatic shear band is formed along the circumference of the tube and the successive stages of the shear band development (nucleation and growth) were investigated. ASB can also be generated by direct impact (Meyers et al., 1991; Klepaczko, 1994; Rittel et al., 2002).

Multiple shear banding can be produced within the wall of a hollow cylinder subject to rapid radial collapse produced by a convergent shock wave (Nesterenko et al., 1994), or by the application of an intense magnetic field (Lovinger et al., 2011). These experiments on hollow cylinders and orthogonal cutting tests share the aptitude of generating multiple shear bands. However, in the case of hollow cylinders shear bands are nucleated almost simultaneously and mutual interactions take place between these bands. On the contrary, in orthogonal cutting shear bands are generated sequentially. After being nucleated at the tool tip an ASB propagates towards the free surface while being convected away from the chip formation region by material flow. There is no interaction between shear bands if each individual band is convected outside from the chip formation region before the next band is formed.

Adiabatic shear banding in machining has been investigated by experimental and theoretical means by Komanduri and Von Turkovich (1981), Molinari et al. (2002) and in several other papers which are presented below. Theoretical results on chip segmentation were derived by Burns and Davies (2002) by means of a one-dimensional continuum model of machining inspired by the early work of Recht (1964). Material failure due to internal damage has been incorporated in numerical simulations of chip serration by using the Johnson–Cook fracture model (Subbiah and Melkote, 2008; Obikawa and Usui, 1996; Atlati et al., 2011). Chen et al. (2011) have performed orthogonal cutting tests for Ti–6Al–4V titanium alloy and have simulated chip serration by using an energy-based ductile failure criterion. From their results, it appears that levels of peaks and valleys of the serrated chip vary nearly in proportion to the feed. Calamaz et al. (2008) have introduced a constitutive law with strain softening to analyze chip segmentation of titanium alloy Ti-6Al-4V.

Orthogonal cutting tests of Ti-6Al-4V titanium have revealed that the chip segmentation frequency is proportional to the cutting speed (Molinari et al., 2002), and decreases with the feed rate (Cotterell and Byrne, 2008). These results were

confirmed by the dry turning experiments of Sun et al. (2009) on Ti-6Al-4V alloy. Atlati et al. (2011) have found similar results by carrying out finite element computations of orthogonal cutting of aluminum alloys.

Modeling of adiabatic shear banding in metal cutting is the subject of the present work. We do not investigate the localized shear zone generated along the tool–chip interface by frictional heating and plastic deformations. This specific problem has been analysed by Molinari et al. (2011, 2012) for continuous cutting processes.

The analysis of chip serration is of practical interest since machining processes are of importance for industrial applications. With some modifications, the results can also be extrapolated to the understanding of chipping at much higher velocities than those realized in machining. Such situations are found in oblique impact of projectiles with metallic substrates, ballistic collision of small particles with planes or aerospace vehicles, accidental interaction of a turbine blade with surrounding components and sharpening by adiabatic shearing of the head of a penetrator (made up of depleted uranium or tungsten alloys) during perforation processes.

We focus on the effect of cutting speed and feed rate on chip serration. ASB are frequently observed during machining of difficult-to-cut metals such as titanium, nickel based alloys and hardened steels (Komanduri and Von Turkovich, 1981). The case of Ti–6Al–4V titanium alloy is considered in this paper. However, the particular choice of the work-material is not of primary importance as we are mostly interested in developing the fundamental knowledge about adiabatic shear banding during cutting and impact processes.

We assume that thermal softening is the sole mechanism triggering shear banding in chip formation. This is frequently the case at high strain rates, but shear banding may be influenced by other softening mechanisms such as dynamic recrystallization, phase transformation or material damage. However, we wish to concentrate on the thermal origin of chip serration. Thermal aspects are of particular importance for Ti–6Al–4V titanium because of its weak thermal conductivity.

Based on finite element computations and analytical considerations, we show that adiabatic shear banding is ruled by simple scaling laws governing the dependence of chip serration upon cutting speed and feed rate. The trends predicted by these scaling laws are thought to be independent of the specific form assumed for the material constitutive law. Several regimes of shear banding are brought to light and the physical aspects related to these regimes are elucidated. Of particular importance is the role played by material convection (due to chip flow) on the evolution of shear bands. This is an important aspect of the originality of the present work with respect to classical analyses of adiabatic shear banding. The results obtained can be useful to other situations where convective flow interferes with the evolution of adiabatic shear bands (impacts and perforation).

2. Problem formulation

2.1. Basic equations

The tool is assumed to be rigid. The work-material is taken as isotropic, elastic–viscoplastic. Plastic flow is governed by the J_2 flow-theory. We do not tackle the task of defining the constitutive law most appropriate to machining operations. Given the high strain rates, large deformations and high temperatures encountered in cutting processes, this task is not an easy one. A simple formulation is adopted here, based on the constitutive law proposed by Johnson and Cook (1983), frequently used for numerical simulations of machining:

$$\sigma_Y = (A + B(\varepsilon_p^{eq})^n)\left(1 + C\ln\frac{\dot{\varepsilon}_p^{eq}}{\dot{\varepsilon}_0}\right)\left(1-\left(\frac{T-T_0}{T_m-T_0}\right)^m\right) \tag{1}$$

σ_Y is the tensile flow stress, $\dot{\varepsilon}_p^{eq}$ the equivalent Mises plastic strain rate, $\varepsilon_p^{eq} = \int \dot{\varepsilon}_p^{eq} dt$ the accumulated plastic strain, T the current temperature, T_0 a reference temperature and T_m the melting temperature. The values of the parameters of the Johnson–Cook law (1) used in our simulations of Ti–6Al–4V alloy are those identified by Lee and Lin (1998), see Table 1. Although the form of the constitutive law, Eq. (1), may appear as too simple for the large range of cutting speeds explored in this work, it will be shown that the predictions of the modeling can be rather well correlated to available experimental results. Therefore, using a simple constitutive law of the form given by Eq. (1) seems at least sufficient for the purpose of characterizing the main trends associated to chip segmentation.

The evolution of temperature in the work-material is governed by the energy equation:

$$\rho C_p \dot{T} - k\Delta T = \beta d_{ij}^p \sigma_{ij} \tag{2}$$

$\dot{T}$ is the material derivative of the temperature and ΔT is the Laplacian of T. By ρ, C_p and k we designate respectively the mass density, the specific heat capacity and the heat conductivity of the work-material. The right hand side of Eq. (2) represents the proportion β of the plastic work converted into heat. d_{ij}^p and σ_{ij} are respectively the components of the plastic

Table 1
Parameters of the Johnson–Cook constitutive law, Eq. (1), for the Ti–6Al–4V alloy according to Lee and Lin (1998).

	A (MPa)	B (MPa)	n	C	m	$\dot{\varepsilon}_0$ (1/s)
Ti6Al4V	782	498	0.28	0.028	1.0	10^{-5}

Table 2
Thermal parameters of Ti–6Al–4V alloy (k, heat conductivity; C_p, specific heat capacity; α, thermal expansion coefficient; T_m, melting temperature).

	k (W/mK)	C_p (J/kg K)	α (μm/mK)	T_m (K)
Ti6Al4V	7.2	560	9.2	1930

strain rate tensor and of the Cauchy stress tensor. Thermal parameters of the Ti–6Al–4V alloy are given in Table 2. The initial temperature, T_0, is equal to 293 K. For keeping the formulation simple, it is assumed that the heat conductivity and the heat capacity are independent of the temperature and that the Taylor–Quinney coefficient is constant and given by $\beta = 0.9$. Other physical quantities are $\rho = 4420$ kg/m^3 (mass density), $E = 114$ GPa (Young's modulus) and $\nu = 0.342$ (Poisson's coefficient).

Mechanical contact at the chip–tool interface is governed by the Coulomb friction law with a constant value of the friction coefficient.

A damage law is frequently brought in for modeling adiabatic shearing in machining (Atlati et al., 2011; Chen et al., 2011). Damage impels a decay of the stress carrying capacity of the work-material that combines itself with the weakening due to thermal softening. In the present paper a simple damage criterion is introduced. A material element is assumed to be undamaged when the accumulated plastic strain ε_p^{eq} is smaller than the critical value ε_{crit} and to be totally damaged (nil resistance) when ε_p^{eq} reaches the value ε_{crit}. It appears that the onset of adiabatic shearing is weakly influenced by the value of ε_{crit}. Thus, adiabatic shear banding in orthogonal cutting of titanium can be triggered without including a damage criterion in the modeling. However, the capacity of the material to deform is limited, and the concept of a critical value of the plastic strain appears as a simple way to account for this limit of material resistance. Another useful aspect granted by the concept of limit strain is to avoid excessive mesh distortion in the finite element computations, as an element is deleted when $\varepsilon_p^{eq} = \varepsilon_{crit}$. It is worth noting that this simple damage criterion was proved to be effective in predicting the failure of ductile materials subject to high loading rates in different situations (fragmentation of thin metallic rings and shells under explosive or blast loadings, failure due to impact loading), see for instance Rusinek and Zaera (2007) and Rodriguez-Martinez et al. (2013). In our problem, fracture is controlled by ε_{crit} and can be triggered by the high level of plastic strain localized within shear bands.

2.2. Dimensional analysis

The link between adiabatic shearing, chip morphology and cutting conditions can be clarified by carrying out a dimensional analysis. Let us denote by L a given characteristic length related to the chip morphology. L may be the average chip thickness, the shear band spacing or the shear band width. Generally, L is function of the cutting conditions (cutting speed V, uncut chip thickness t_1, rake angle α, tool edge radius R, see Fig. 2), and depends also on the physical and mechanical properties of the work-material: mass density, ρ; parameters of the Johnson–Cook law, Eq. (1), A, B, n, C, $\dot{\varepsilon}_0$, m, T_0, T_m; elastic constants (Young's modulus, E; Poisson's ratio, ν); thermal parameters (heat conductivity, k; heat capacity, C_p). Tool–chip interface characteristics are also involved (sliding friction coefficient, μ; thermal compliance, κ). The tool is assumed to be non-deformable. Thus, only its thermal properties $\left(k_T,\ C_p^T\right)$ are considered.

Dimensional analysis and application of the Vaschy–Buckingham Π-theorem show that L is related to other parameters through the following relationship involving dimensionless numbers:

$$\frac{L}{t_1} = g\left(R_k, R_\kappa, R_h, R_I, R_{rate}, \frac{k}{k_T}, \frac{\rho C_p}{\rho_T C_p^T}, \alpha, \frac{R}{t_1}, \frac{A}{E}, \frac{B}{E}, \nu, n, C, m, \frac{T_m}{T_0}, \mu\right) \tag{3}$$

with

$$R_k = \frac{\rho C_p t_1 V}{k},\ R_\kappa = \frac{\rho C_p V}{\kappa},\ R_h = \frac{\beta A}{\rho C_p T_m},\ R_I = \frac{\rho V^2}{A},\ R_{rate} = \frac{V}{t_1 \dot{\varepsilon}_0} \tag{4}$$

R_k is inversely proportional to the heat conductivity of the work-material. R_κ is the dimensionless thermal resistance of the tool–chip interface (κ being the interface conductance). R_h characterizes the internal heating due to plastic deformation of the work-material. We note that β features the proportion of plastic work converted into heat and that the yield stress of the work-material is calibrated by the parameter A; therefore, βA scales the amount of dissipated heat energy. R_I characterizes inertia effects and R_{rate} represents the effects of material rate sensitivity. R/t_1 is the normalized tool edge radius.

The characteristics of the work-material and those of the interface (μ and κ) are kept constant. The rake angle α is zero. Only the cutting speed V , the feed t_1 and the edge radius R are varied. Therefore, by omitting the parameters that are not dependent upon V, t_1 and R, Eq. (3) can be written as

$$\frac{L}{t_1} = g\left(R_k, R_\kappa, R_I, R_{rate}, \frac{R}{t_1}\right) \tag{5}$$

Adiabatic conditions are fulfilled when R_k and R_κ are large, i.e. when k and κ are tending to zero, or when the cutting speed V is high.

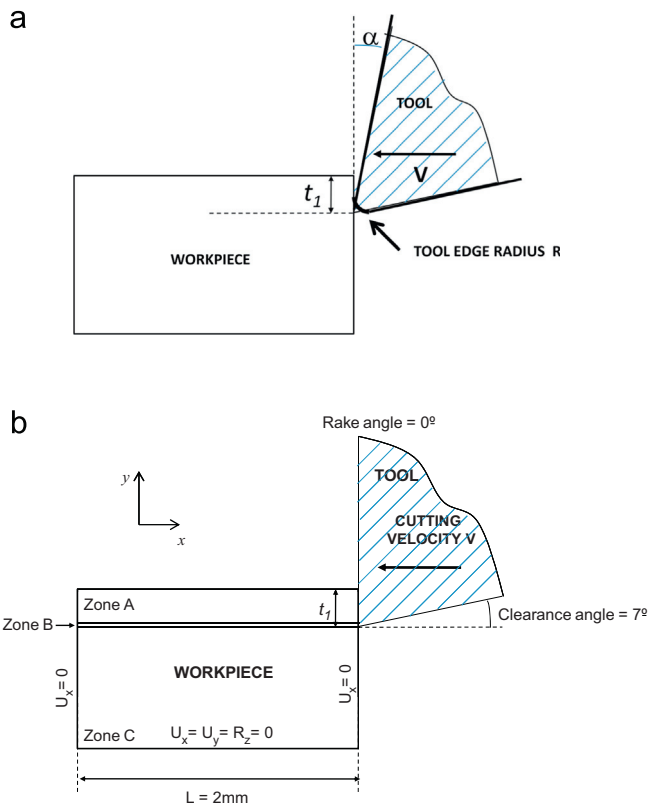

Fig. 2. (a) Orthogonal cutting configuration, (b) decomposition of the workpiece in different zones A, B and C. The damage parameter ε_{crit} has the value 2 in the separation layer B. In most of calculations the value $\varepsilon_{crit} = 8$ is assigned to zones A and C, but this value may be changed in order to investigate the effect of the damage parameter on chip segmentation.

The effects of material inertia are carried by R_I. These effects become significant when the cutting speed is large. Interestingly, there exists a range of intermediate cutting speeds, $V_{inf}(L) < V < V_{sup}(L)$ (a priori function of the characteristic length L of the phenomenon under consideration), for which inertia effects can be neglected (because the velocity is not too large) and heat transfer effects are also negligible (since the velocity is not too small). These features are clearly seen in the numerical modeling of chip formation and will be exemplified later. $V_{inf}(L)$ represents the cutting speed above which heat transfer effects are negligible at the scale L, while $V_{sup}(L)$ marks the limit above which inertia effects become important.

For $V_{inf}(L) < V < V_{sup}(L)$, the characteristic length L is related to cutting conditions by Eq. (5) where the dependence upon R_k, R_κ and R_I can be omitted:

$$\frac{L}{t_1} = g\left(R_{rate}, \frac{R}{t_1}\right) = g\left(\frac{V}{t_1 \dot{\varepsilon}_0}, \frac{R}{t_1}\right) \tag{5′}$$

We note that the ratio L/t_1 remains unaltered when the feed, t_1, the tool edge radius, R, and the cutting velocity, V, are changed in same proportions: $t_1 \to \lambda t_1$, $R \to \lambda R$, $V \to \lambda V$, where λ is a scaling factor. This observation is in keeping with experimentally and theoretically established scaling laws in high speed machining (Sutter et al., 2012).

2.3. Numerical model

A plane strain model of orthogonal cutting is developed using the Finite Element code ABAQUS/Explicit with Lagrangian formulation. A thermo-mechanical coupled analysis is carried out by considering CPE4RT elements, see Abaqus Manual (2003). Those are plane strain, quadrilateral, linearly interpolated, and thermally coupled elements with reduced integration and automatic hourglass control.

The basic geometry of the numerical model is presented in Fig. 2b. Except otherwise specified, a sharp tool edge is considered. The workpiece is fixed at the lowest contour and the cutting speed is applied to the tool. The mesh of the workpiece is divided in three different zones. The layer of material which will be removed by cutting is composed of zone A (main part) and zone B (thin bottom layer of 4 μm thickness). The upper limit of zone C corresponds to the machined surface. The mesh at zones B and C is parallel to horizontal and vertical directions, while the mesh at the zone A is characterized by an inclination angle θ with the horizontal direction. The orientation of the mesh is aimed to facilitate the

formation of segmented chip during orthogonal cutting of Ti alloys (Hortig and Svendsen, 2007; Soldani et al., 2010). It will be shown in Appendix A that an optimal orientation is given by $\theta = = 45^\circ$.

No remeshing technique is used. However, the nominal element size is varied from 1 μm to 8 μm in order to check the convergence of results, Appendix A.

An element is deleted when $\varepsilon_p^{eq} = \varepsilon_{crit}$. The level of the erosion parameter is taken as $\varepsilon_{crit} = 8$ in both zones A and C and is assigned a lower value $\varepsilon_{crit} = 2$ in zone B in order to allow for easy separation between chip and substrate. The value of ε_{crit} in zone A will be varied to check the impact of this damage parameter on chip serration.

Except otherwise specified, calculations are conducted with $\varepsilon_{crit} = 8$ in zones A and C, mesh orientation $\theta = 45^\circ$ in zone A and with nominal mesh size $\delta = 1.5\ \mu m$ for $t_1 = 50\ \mu m$; $\delta = 3\ \mu m$ for $t_1 = 100\ \mu m$ and $\delta = 5\ \mu m$ for $t_1 = 250\ \mu m$.

3. Analysis of chip segmentation and chip morphology

Numerical simulations of adiabatic shear banding in orthogonal cutting are analyzed and compared to experimental data obtained for Ti–6Al–4V alloy. The effects of the cutting speed and of the uncut chip thickness (feed) are discussed. The rake angle is zero in all simulations and the sliding friction coefficient has a fixed value $\mu = 0.4$.

3.1. Characterization of the chip morphology

A view of a serrated chip obtained from Finite Element simulations is displayed in Fig. 3a. The cutting speed, the uncut chip thickness are respectively $V = 4\ \mathrm{ms}^{-1}$ and $t_1 = 0.1$ mm. The chip appears to be divided into small segments delimited by nearly regularly spaced shear bands. The chip morphology will be mostly analysed along the flat rake face of the tool. Chip curling is not studied here.

An idealized view of the chip along the rake face is presented in Fig. 3b. The morphology is characterized by four parameters: the characteristic spacing between shear bands L_s, the shear band inclination ϕ_s, the maximum and minimum chip thicknesses (i.e. peak and valley levels) , respectively t_2^+ and t_2^-. ϕ_s is the final orientation of shear bands which is different from the orientation at the onset of shear banding. ϕ_s is not an independent parameter as it is related to t_2^+ and t_2^- by Eq. (7). It should be noted that the chip morphology in Fig. 3a is not as regular as in Fig. 3b. Indeed, L_s, ϕ_s, t_2^+ and t_2^- have to be viewed in Fig. 3b as average values along the chip. For L_s this aspect will be specified later.

The length of the chip segment, L_1 (see Fig. 3b), and the average chip thickness, $\bar{t}_2$, are respectively defined by

$$L_1 = L_s/\cos\phi_s, \quad \bar{t}_2 = \frac{1}{2}(t_2^+ + t_2^-), \tag{6}$$

This definition of the average chip thickness is consistent if we assume that peaks and valleys are triangular shaped as in Fig. 3b. Then, the volume of the chip is given by $\bar{t}_2 * (\textit{chip length})$. Also, ϕ_s is related to the mean chip thickness by

$$\phi_s = \arctan(t_1/\bar{t}_2) \tag{7}$$

In the absence of shear instability, we have $t_2^+ = t_2^- = t_2$, where t_2 is the chip thickness.

Fig. 3c is an enlarged view of the segmented chip obtained at a different time from those of Fig. 3a. Fluctuations are observed in the serration pattern and shear bands are curved. Thus, characterizing the shear band spacing is not straightforward. In fact, the distance between shear bands appears to be smaller near the free surface than nearby the tool. Therefore, two measures of the spacing are introduced, resp. L_s^- and L_s^+. Let us denote by Band1 and Band2 two neighboring bands, see Fig. 3c. Point A is located within Band1 at the valley bottom and in the middle of the band. $L_s^- = AA'$ is the distance between A and the middle line of Band2. L_s^- represents roughly a measure of the distance between two valleys.

Point B is located at the center of Band2 at the tool–chip interface. $L_s^+ = BB'$ is the distance between B and the middle line of Band1. As AA' (resp. BB') varies along the chip, L_s^- (resp. L_s^+) is viewed as an average value of AA' (resp. BB') along the chip. Finally, the mean shear band spacing is defined as

$$L_s = \frac{1}{2}(L_s^- + L_s^+) \tag{8}$$

In the ideal case of regular straight parallel shear bands as in Fig. 3b, we have $L_s = L_s^- = L_s^+$, and L_s is simply the distance between the neighboring bands.

The intensity of the localization process along shear bands is characterized by the segmentation index, S_i, defined as

$$S_i = (t_2^+ - t_2^-)/t_2^+ \tag{9}$$

In the case of irregular chip segments (Fig. 3c), t_2^+ (resp. t_2^-) is taken as the average value of the distance between peaks (resp. valleys) and the opposite surface of the chip.

It was observed in our simulations that the chip could be fragmented at high cutting speeds by crack propagation along shear bands. In this case S_i was evaluated by considering the chip morphology prior to fragmentation of the chip. In other words, if a crack is developing, t_2^- is not referring to the crack tip position but rather to the valley bottom from which the crack is initiated.

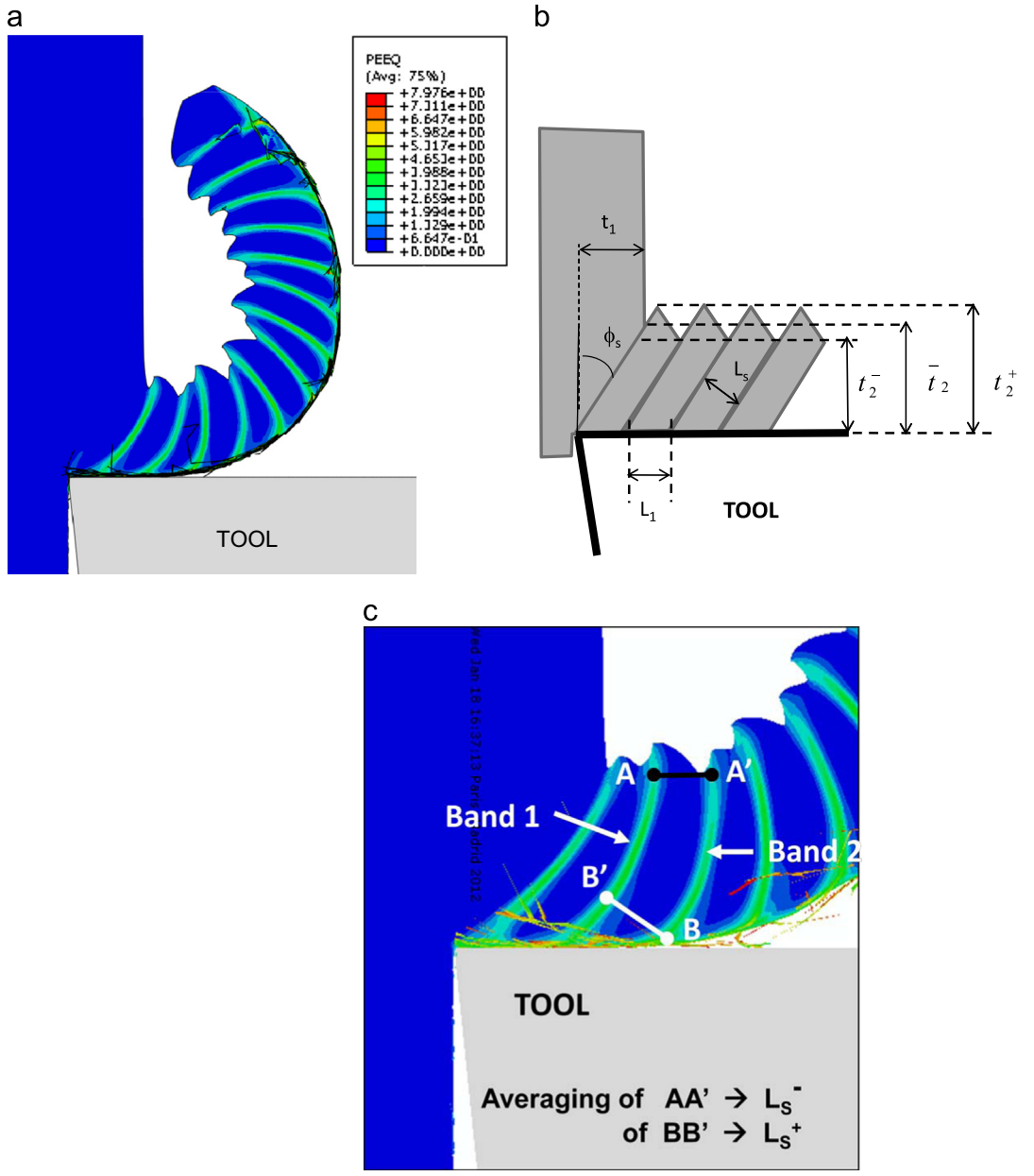

Fig. 3. (a) Chip morphology obtained for orthogonal cutting of Ti–6Al–4V alloy with FEM simulations. The cutting speed, the feed and the rake angle are respectively $V = 4$ ms^{-1}, $t_1 = 0.1$ mm and $\alpha = 0$. Calculations are conducted for a mean mesh size of 3 μm and the value $\varepsilon_{crit} = 8$ of the critical plastic strain. (b) Idealized view of a regularly segmented chip with definition of the shear band spacing L_s and of the levels of peaks and valleys t_2^+ and t_2^-. (c) Characterization of $L_s^+ = BB'$ and $L_s^- = AA'$. Since the pattern of chip segmentation is not quite regular, L_s^+ and L_s^- are respectively average values of BB' and AA' along several chip segments.

Shear band**s** observed during machining of Ti–6Al–4V have a thickness of few micro-meters (Komanduri and von Turkovich, 1981; Molinari et al., 2002). A fine mesh must be used to capture the high level of strain localization in these narrow zones. Convergence of the computations is checked in Appendix A by considering decreasing mesh sizes up to 1 μm.

3.2. Conditions for the onset of adiabatic shearing

Simulations show the existence of a speed, V_{segm}, marking the transition from uniform chip to segmented chip. No shear banding is observed for cutting speeds below V_{segm}. Flow instability and shear banding are activated for $V > V_{segm}$ because effects of heat diffusion are slowed down when the cutting speed is increased. Then, localized heating and plastic flow localization are promoted. There is no need for true adiabatic conditions to activate shear banding. Diminishing heat transfer

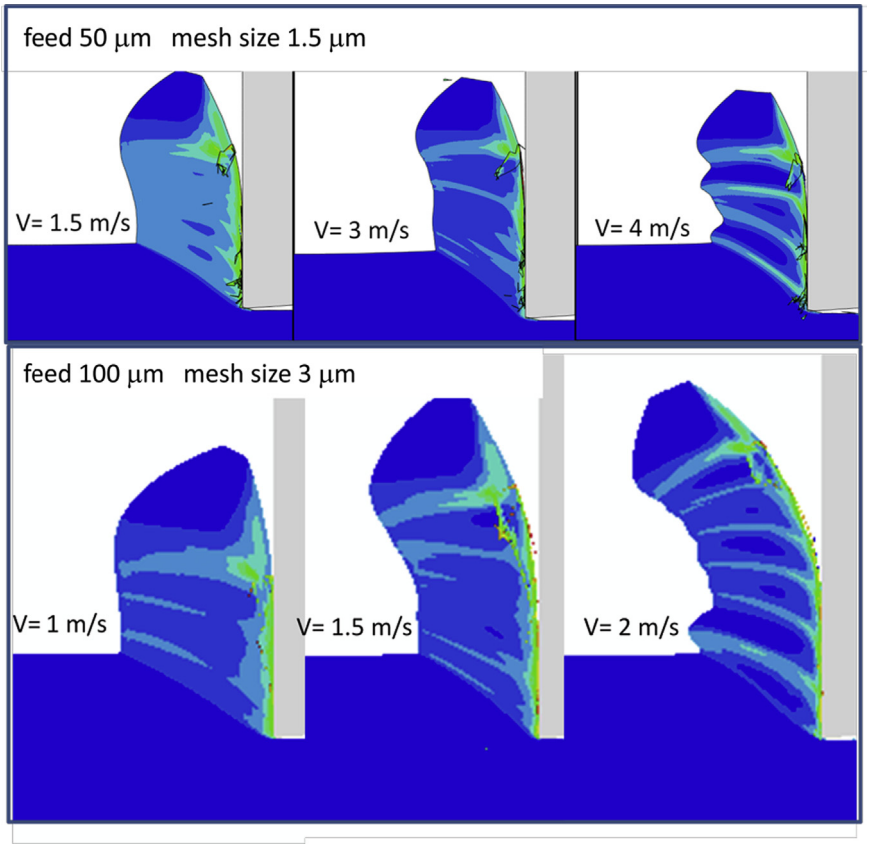

Fig. 4. Evolution of the chip morphology for increasing cutting speeds and two values of the feed ($t_1 = 50$ and $100\ \mu m$). The transition speed V_{segm} to chip segmentation is observed to be about $V_{segm} \approx 3\ ms^{-1}$ for $t_1 = 50\ \mu m$ and $V_{segm} \approx 1.5\ ms^{-1}$ for $t_1 = 100\ \mu m$.

effects is enough. According to Childs (2013), the occurrence of thermal shear bands in metal cutting is ruled by a critical value R_k^{segm} of the normalized cutting speed R_k (also denoted as "thermal number" by Childs, 2013). Considering the definition of R_k, Eq. (4), the onset of chip serration is characterized by the transition speed:

$$V_{segm} = kR_k^{segm}/\rho C_p t_1 \tag{10}$$

The transition between continuous chip and segmented chip is illustrated in Fig. 4. Chip morphologies are displayed for several values of cutting speed and feed. The speed characterizing the onset of flow instability can be estimated as $V_{segm} \approx 3\ ms^{-1}$ for $t_1 = 50\ \mu m$, $V_{segm} \approx 1.5\ ms^{-1}$ for $t_1 = 100\ \mu m$ and $V_{segm} \approx 0.7\ ms^{-1}$ for $t_1 = 250\ \mu m$ (chip morphology not shown in this case). It is checked that V_{segm} is approximately ruled by Eq. (10) with $R_k^{segm} = 40$. The value $R_k^{segm} = 40$ characterizing the transition to chip serration will be confirmed later by the evolution of the segmentation index versus R_k shown in Fig. 13a.

Following Eq. (10), it appears that V_{segm} is inversely proportional to t_1. This is in keeping with the "chip load criterion" introduced by Bayoumi and Xie (1995) assuming that chip serration is triggered when Vt_1 reaches a critical value. According to Eq. (10), this critical value is proportional to the thermal diffusivity $k/\rho C_p$ of the work material if the same critical value $R_k^{segm} = 40$ is assumed to control the transition to chip serration for metals.

It should be recalled that chip segmentation is ruled by thermal softening in the present modeling. However, at low cutting speeds, other softening mechanisms such as material damage or dynamic recrystallization may also trigger chip flow instabilities. This point will be further discussed in Section 3.7.

3.3. Shear band spacing: subcritical regime

The formation of thermal shear bands is governed by distinct regimes depending on the level of the cutting speed. The subcritical regime of shear banding occurs for cutting speeds lower than a critical value V^+ which is characterized in Section 3.4. In this regime, shear bands propagate through the entire chip thickness. After being nucleated at the tool tip, a shear band is fully developed and a high level of strain localization is reached within the band. Because of the significant unloading that results from this intense localization process, there is no possibility to nucleate a new band before the

previous one has been convected away from the chip formation region. Therefore, direct interaction between successive shear bands cannot take place.

Above V^+ (supercritical regime) we report the existence of a totally different mechanism of adiabatic shear banding involving important inertia effects, an abrupt drop of the shear band spacing and significant interactions between shear bands.

Fig. 5a shows the evolution of the normalized shear band spacing L_s/t_1 in terms of the normalized cutting speed $R_k=\rho C_p t_1 V/k$ for three values of the feed t_1. It is recalled that L_s is defined by Eq. (8), with L_s^+ and L_s^- being average values characterized in Fig. 3c. As said in Section 2.3 and discussed in Appendix A, to insure the accuracy of numerical simulations for L_s the mesh size is $\delta=1.5\ \mu m$ for $t_1=50\ \mu m$, $\delta=3\ \mu m$ for $t_1=100\ \mu m$ and $\delta=5\ \mu m$ for $t_1=250\ \mu m$.

At low speed, we observe in Fig. 5a an increase of the shear band spacing followed by a plateau where L_s/t_1 is almost independent from cutting speed and feed.

These trends are in agreement with the experiments performed on hardened steels by Davies et al. (1997) who reported that by increasing the cutting speed the normalized spacing L_s/t_1 becomes periodic, increases and finally approaches an asymptotic value (corresponding to our plateau regime).

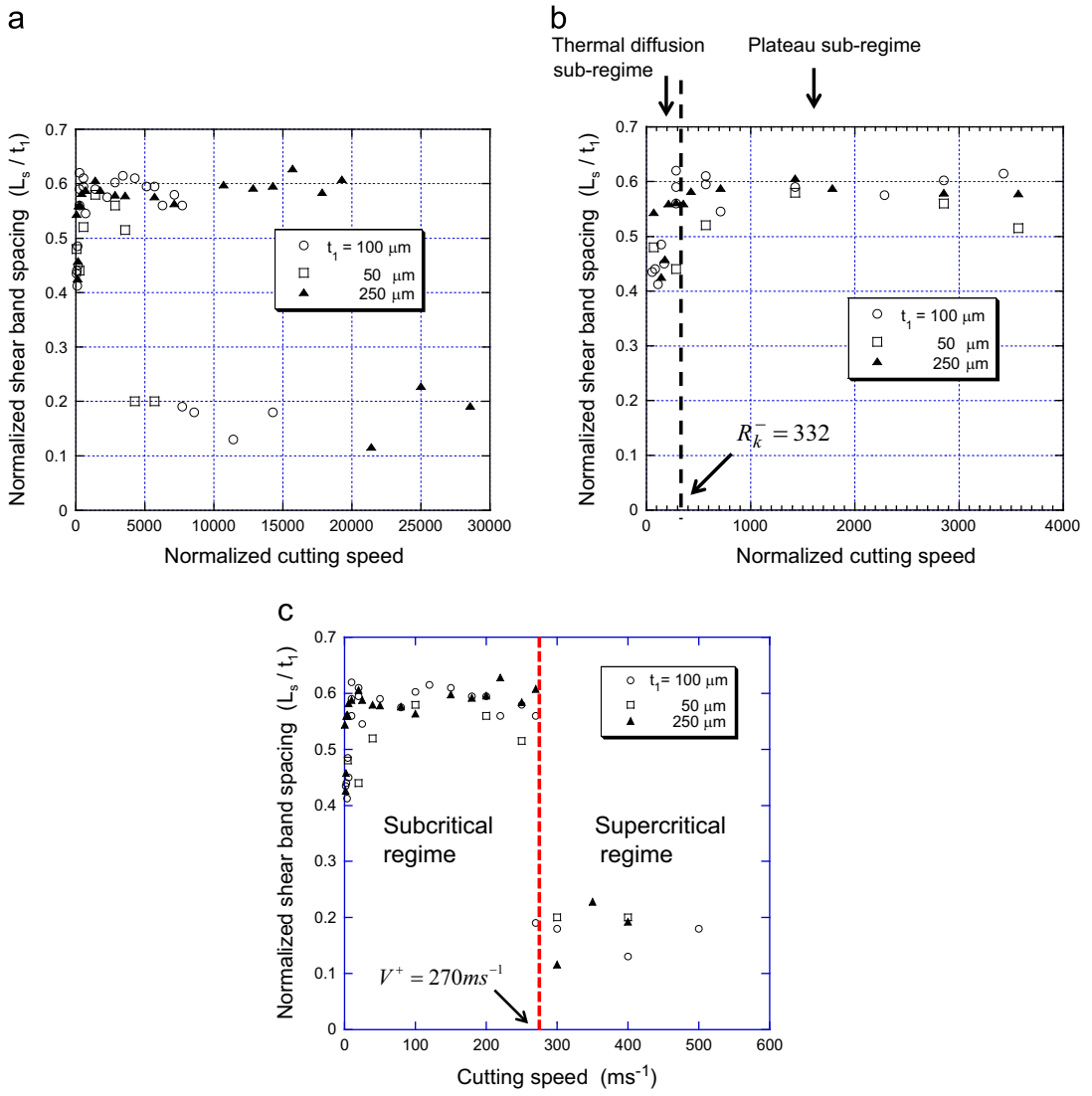

Fig. 5. (a) Normalized shear band spacing L_s/t_1 in terms of the normalized cutting speed $R_k=\rho C_p t_1 V/k$, (b) within the subcritical regime ($V<V^+=270\ \mathrm{ms}^{-1}$) two sub-regimes can be distinguished. Heat transfer effects are effective in the thermal diffusion sub-regime and negligible (at the scale of the shear band spacing L_s) in the plateau sub-regime. The transition between the thermal diffusion sub-regime and the plateau sub-regime occurs for the value $R_k^-=332$. Note that the normalized shear band spacing is independent of cutting speed and feed in the plateau sub-regime. (c) Normalized shear band spacing L_s/t_1 in terms of the cutting speed V. Note the sudden drop of the shear band spacing at V^+. The supercritical regime of shear band spacing is defined by $V>V^+$ and the subcritical regime by $V<V^+$.

It can be noted that for a smaller feed the plateau is less extended in terms of the normalized cutting speed R_k (Fig. 5a) but has same extension in terms of the cutting speed (Fig. 5c). Indeed, the end of the subcritical regime is characterized by the critical velocity $V^+ = 270\ \mathrm{ms}^{-1}$ which is independent of the feed. For $V > V^+$ the shear band spacing is drastically reduced (supercritical regime discussed in Section 3.4).

Two sub-regimes of shear band spacing can be defined within the subcritical regime $(V < V^+)$. At relatively low cutting speeds $V < V^-$ (thermal diffusion sub-regime), the shear band spacing is affected by heat conduction. Following the dimensional analysis of Section 2.2, L/t_1 is given by Eq. (5). For a rate independent work-material we have $C=0$ in the Johnson–Cook law, Eq. (1), and the effect of the parameter $\dot{\varepsilon}_0$ disappears. Thus L/t_1 does not depend on $R_{rate} = V/t_1\dot{\varepsilon}_0$. The rate sensitivity of Ti–6Al–4V titanium being rather weak, the contribution of R_{rate} in Eq. (5) will be neglected.

Except otherwise specified, the tool edge is assumed to be sharp. Therefore, $R/t_1 = 0$ in Eq. (5). The effect of the tool edge radius will be investigated in Fig. 9.

With the above assumptions of weak rate sensitivity and sharp tool, Eq. (5) with $L = L_s$ can be simplified as

$$L_s/t_1 = g(R_k, R_I) \tag{11}$$

R_κ is not included in Eq. (11) since the effect of the thermal compliance of the tool–chip interface on shear band spacing appears to be negligible.

Based on Eq. (11), a rational interpretation of the results obtained at various feeds and cutting speeds can be proposed. At low cutting speeds (thermal diffusion sub-regime) inertia plays no role but heat conduction effects are operant. Consequently L_s/t_1 is solely function of R_k:

$$\frac{L_s}{t_1} = g\left(\frac{\rho C_p t_1 V}{k}\right) \tag{12}$$

This relationship explains why the results displayed in Fig. 5a for various cutting speeds and feeds are nearly grouped along a single master curve at low values of R_k.

By increasing the cutting speed, the effect of heat conduction on shear band spacing declines until being ineffective on the plateau seen in Fig. 5b (plateau sub-regime). In this case, Eq. (12) reduces to

$$L_s/t_1 = const \tag{13}$$

The shear band spacing is independent of cutting speed and is proportional to the feed.

The transition to the plateau sub-regime is controlled by the thermal number R_k. Beyond a critical value R_k^- the effects of heat transfer are inoperative on the shear band spacing L_s. But it would be ambiguous to qualify the process as truly adiabatic since heat flow remains effective at the shear-band level. At the most, the process can be viewed as adiabatic at the scale L_s.

The transition to the plateau regime takes place around the velocity:

$$V^- = kR_k^-/\rho C_p t_1 \tag{14}$$

From our simulations the transition velocity is $V^- = 20\ \mathrm{ms}^{-1}$ for $t_1 = 50\ \mu m$, $V^- = 10\ \mathrm{ms}^{-1}$ for $t_1 = 100\ \mu m$ and $V^- = 3\ \mathrm{ms}^{-1}$ for $t_1 = 250\ \mu m$. These values of V^- are compared in Fig. 6 to the prediction of Eq. (14) with $R_k^- = 332$ (noting that the value $k/\rho C_p = 2.9\ \mathrm{mm}^2\mathrm{s}^{-1}$ was used for Ti6Al4V). Thus, the transition to adiabatic conditions (at the scale L_s) appears to be ruled by the value $R_k^- = 332$ of the thermal number and the transition velocity V^- is inversely proportional to the feed t_1 (Eq. (14) and Fig. 6).

3.4. Shear band spacing: supercritical regime

Beyond V^+ (supercritical regime) a totally different mechanism of adiabatic shear banding is activated. Shear bands do not cross the entire chip thickness, an abrupt drop of the shear band spacing L_s is observed (Fig. 5a and b), several shear bands are simultaneously growing within the chip formation region and these bands interact mutually. It will be seen that these aspects are related to inertia effects which become significant at very high cutting speeds.

When L_s is displayed in terms of the cutting speed, as in Fig. 5c, it appears that the transition to the supercritical regime occurs at the cutting speed $V^+ \approx 270\ \mathrm{ms}^{-1}$ (for Ti–6Al–3V). It is noticeable that V^+ is nearly insensitive to the feed.

Cutting speeds of the order of V^+ or higher are not achieved at present in current machining operations. Notwithstanding, the problem has an interest in other contexts, including impact problems. In particular the sharpening of the head of a penetrator (made up of depleted uranium or tungsten alloys) during perforation is due to adiabatic shear banding, and this process bears some similarity with adiabatic shearing in metal cutting operations.

For $V > V^+$, the shear band spacing is drastically reduced to a small fraction of the feed of the order of $L_s/t_1 \approx 0.2$. The spacing is small enough so that shear bands can interact before they are moved away from the chip formation region (primary shear zone). This is a notable difference with the subcritical regime $(V < V^+)$ where shear bands are formed sequentially without interfering between each other. On the contrary, in the supercritical regime $(V > V^+)$ a new band is formed while the previous band is still active.

The phenomena observed in the supercritical regime are due to inertia effects. This causality is supported by various arguments. Firstly, we note that inertia effects are embodied in the dimensionless inertial number $R_I = \rho V^2/A$. Thus, the idea

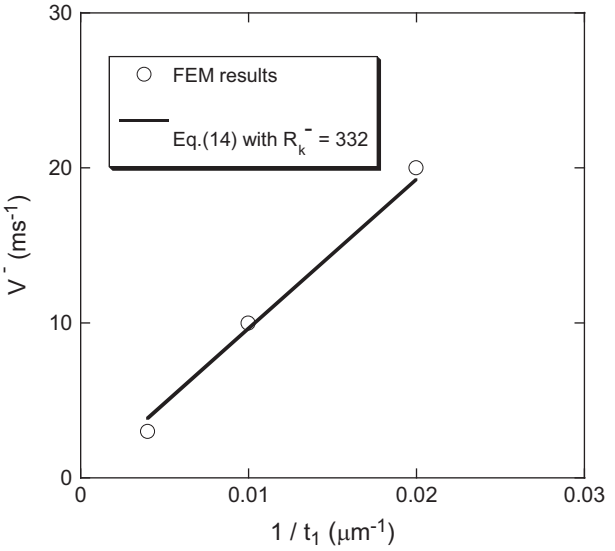

Fig. 6. Cutting speed V^- in terms of the inverse of the feed. V^- is the transition speed between the thermal diffusion sub-regime ($V < V^-$) and the plateau sub-regime. Dots represent FEM results, and the continuous line is the prediction given by Eq. (14) with $R_k^- = 332$. It is seen that V^- is inversely proportional to the feed t_1.

that the transition to the supercritical regime is controlled by inertia, i.e. by a critical value R_I^+ of the inertial number, bears out the observation that the critical speed V^+ is insensitive to the feed t_1 (Fig. 5c). According to the idea that the transition is governed by R_I^+, the critical velocity would be $V^+ = \sqrt{R_I^+ A/\rho}$, thus depending on the mass density, ρ, and on the yield resistance of the work-material (related to parameter A), but being independent from the feed t_1.

To support further the role of inertia with respect to the occurrence of the supercritical regime, we refer to the problem of multiple shear banding arising during the rapid radial collapse of hollow cylinders subject to a radial compressive shock wave (Nesterenko et al., 1994). In this process, the material sustains nominal shear rates of the order of 10^4 s^{-1}. A family of adiabatic shear bands is spontaneously formed. Using a linearized perturbation approach, it was theoretically demonstrated that the shear band spacing declines when the overall applied strain rate is increased (Wright and Ockendon, 1996; Molinari, 1997). This effect is due to inertia which impedes the growth of long wavelength perturbations (Molinari, 1985).

However, we should be cautious when transposing these results to orthogonal cutting. During the collapse of cylinders the whole set of shear bands is activated almost simultaneously and therefore mutual interactions between shear bands can be effective. Instead, as mentioned before, in machining shear bands are formed sequentially and are convected away from the chip formation region. Nonetheless, our numerical simulations show that, at very high cutting speeds ($V > V^+$), several shear bands are simultaneously active in the chip formation region. These shear bands interact and the resulting trends can be investigated with a linearized perturbation approach. Such a perturbation analysis was attempted by Molinari et al. (2002) in the context of machining, but very high cutting speeds should be explored experimentally to validate the theoretical results.

Results of the linearized stability analysis indicate that, when shear bands interact, the band spacing is a decreasing function of the applied nominal strain rate. This is a general feature that is supported by experimental results and theoretical analyses (Wright and Ockendon, 1996; Molinari, 1997). The shear band spacing L_s is displayed in Fig. 7a in terms of the strain rate measure V/t_1 for $V > V^+$ and for several feeds. L_s appears as a decreasing function of the strain rate in agreement with the theoretical predictions. It should be noted that the nominal shear rate $\dot{\gamma}$ applied to the primary shear zone (chip formation region) is scaled by V/t_1 if we assume that the thickness of this zone is of the form $w_{PSZ} = at_1$ with the factor a being constant. This scaling law was experimentally and theoretically verified at high cutting speeds by Sutter et al. (2012).

It was established in Section 3.3 that adiabatic conditions are prevailing at the scale of the shear band spacing in the plateau regime. However, because of the important decay of L_s observed for $V > V^+$, heat conduction effects can affect the band spacing in the supercritical regime. By using a linearized perturbation analysis it results that the shear band spacing is ruled by the following scaling law (Wright and Ockendon, 1996; Molinari, 1997; Molinari et al., 2002):

$$L_s \approx \left(\frac{m^3 k \rho C_p {T_0}^2}{\rho \beta^2 \dot{\gamma}^3 \tau_0 \nu^2} \right)^{1/4} \tag{15}$$

This result was derived for a non-hardening material obeying the following constitutive law:

$$\tau = \tau_0 \left(\frac{\dot{\gamma}}{\dot{\gamma}_0} \right)^m \left(\frac{T}{T_0} \right)^\nu . \tag{16}$$

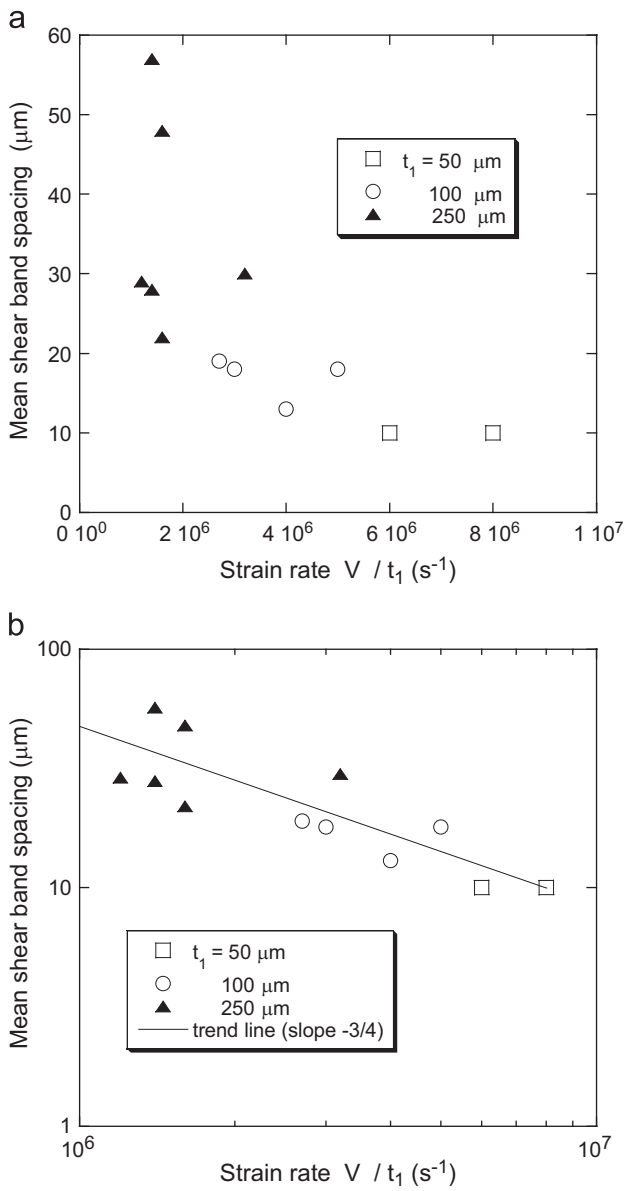

Fig. 7. (a) Mean shear band spacing L_s in terms of the strain rate V/t_1 (which scales with the strain rate within the primary shear zone). Cutting speeds are in the supercritical regime $V > V^+$. (b) Log–log diagram showing that L_s is scaled by $(V/t_1)^{-3/4}$ as predicted by the linearized stability analysis.

where τ is the shear flow stress and $\dot{\gamma}$ is the shear rate. The analysis can be also extended to the case of hardening materials (Molinari, 1997) but to investigate the effect of the strain rate, the simple approach based on Eq. (15) is sufficient . In terms of dimensionless numbers, Eq. (15) can be expressed as

$$L_s \approx \left(\frac{m^3 R_k}{\nu^2 R_h^2 R_I}\right)^{1/4} \tag{17}$$

This relationship illustrates the contribution of heat conduction (R_k), heat generation (R_h) and inertia (R_I) to the shear band spacing in the supercritical regime. From Eq. (15), we note that $L_s \propto \dot{\gamma}^{-3/4}$. In the context of orthogonal cutting, $\dot{\gamma}$ is the nominal shear rate applied to the chip formation region (primary shear zone) which is scaled by V/t_1 as seen above. Therefore, the following scaling law is obtained:

$$L_s \propto \left(\frac{V}{t_1}\right)^{-3/4} \tag{18}$$

The trend predicted by the linearized stability analysis is in agreement with the numerical results displayed in Fig. 7b showing L_s versus V/t_1 in a log–log scale (slope (−3/4)).

A second approach, based on the momentum diffusion theory of shear band spacing of Grady and Kipp (1987) and Grady (1992), would provide the same power law dependence with respect to strain rate as in Eq. (15). Therefore, both approaches (linear perturbation and momentum diffusion) provide the same dependence of the shear band spacing with respect to the nominal shear rate. We refer to Zhou et al. (2006b) for a comprehensive analysis of the formation of multiple shear bands and a critical review of analytical approaches.

Ye et al. (2013) have theoretically analyzed the formation of shear bands in high speed machining by adapting the momentum diffusion theory to the context of metal cutting. They predicted a decreasing of the shear band spacing with the cutting speed. However, our numerical calculations show a decreasing of the shear band spacing for higher values of the cutting speed than those predicted by Ye et al. (2013).

One should recall that in the subcritical regime $(V < V^+)$ each band is formed independently with no interaction with the other bands. In this case the scaling law (18) does not apply.

3.5. Shear band spacing: comparison with experimental results

Experimental data on shear band spacing are reported in Table 3 and are displayed in Fig. 8. These data are rather well correlated with simulation results. High cutting speeds were experimentally explored by Gente and Hoffmeister (2001) and Bäker et al. (2002). Lower speeds were considered by Chen et al. (2011) with a rake angle of 3°. However, this angle is small enough for meaningful comparison with our simulations carried out with $\alpha=0$. The values of L_s given in Table 3 were estimated from our own measurements on chip morphologies reported in Gente and Hoffmeister (2001), Bäker et al. (2002) and Chen et al. (2011).

It should be noted that simulations were carried out with a sharp tool. To better compare experiments and modeling, the influence of the tool edge radius is investigated in Fig. 9. L_s/t_1 is displayed in terms of the normalized cutting speed $R_k$for a tool edge radius of 25 μm and a sharp tool. The feed is $t_1 = 100\ \mu m$. The shear band spacing appears to be an increasing function of R. Thus, by taking account of the tool edge-radius the simulation results would be shifted upwards in Fig. 8

Table 3
Cutting conditions and experimental data for orthogonal cutting of Ti–6Al–4V from Chen et al. (2011) (tests #1–2), Gente and Hoffmeister (2001) (#3 and 5), Bäker et al. (2002) (#4).

Test #	Cutting speed, V (ms^{-1})	Feed, t_1 (μm)	Rake angle, α (deg)	Mean shear band spacing, L_s (μm)
1	2.85	150	3	89
2	4.2	100	3	56
3	20	70	0	40
4	40	42	0	27
5	80	35	0	22

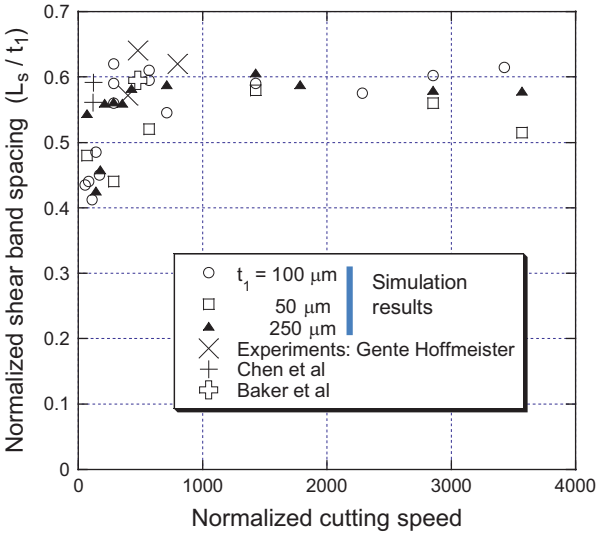

Fig. 8. Normalized shear band spacing L_s/t_1 in terms of the normalized cutting speed $R_k = \rho C_p t_1 V/k$ (as in Fig. 5b). Experimental data of Chen et al. (2011), Gente and Hoffmeister (2001) and Bäker et al. (2002), reported in Table 3, are compared to simulation results.

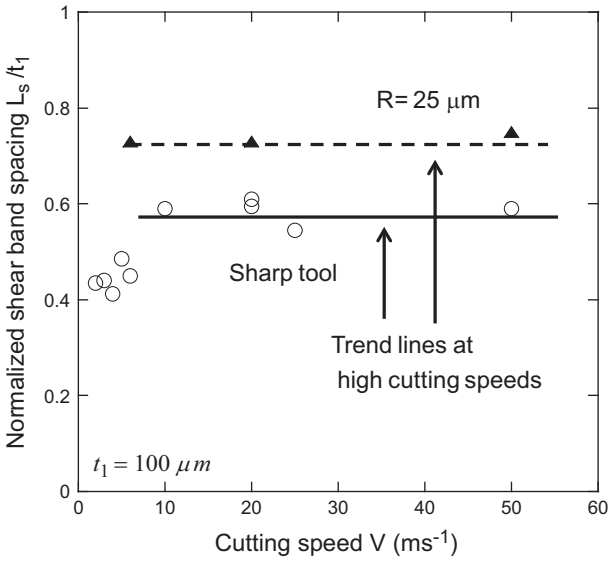

Fig. 9. Effect of the tool edge radius. An increase of about 20% of the shear band spacing is seen for the rounded tool edge ($R = 25\ \mu m$) as compared to the perfectly sharp tool ($R = 0$). The feed is $t_1 = 100\ \mu m$.

(by about 20% for a tool with $R = 25\ \mu m$) . This effect would even improve the quality of the correlation between simulations and experimental data.

3.6. Mean chip thickness

The characteristic length L considered in this section is the mean chip thickness $\bar{t}_2$. The same analysis applies as for the mean shear band spacing L_s. Fig. 10 shows, in semi-logarithmic scale, the dependence of $\bar{t}_2/t_1$ with respect to the normalized cutting speed $R_k = \rho C_p t_1 V/k$ for several values of the feed. As in Fig. 5b, we note the existence of a plateau where $\bar{t}_2$ is nearly independent of V and is proportional to the feed t_1. However, the plateau extends to velocities larger than V^+.

Data corresponding to several feeds and cutting speeds are gathered in a single master curve. This is a proof that the mean chip thickness (and therefore also the final shear band orientation $\phi_s = \arctan(t_1/\bar{t}_2)$) is mostly controlled by heat transfer effects. These effects are embedded in R_k through the heat conductivity k . The transition to the plateau sub-regime occurs at the same value $R_k^- = 332$ as for L_S/t_1, see Fig. 5b. The plateau observed at high cutting speeds is related to adiabatic conditions at the scale $\bar{t}_2$ (as for L_s).

3.7. Frequency of segmentation

Shear banding causes oscillations of the cutting force. The period of oscillations is the time interval $(\Delta t)_{force}$ between two successive peaks of the force (associated to successive bands). The frequency of oscillations is defined as

$$f_{force} = 1/(\Delta t)_{force} \tag{19}$$

$(\Delta t)_{force}$ can be estimated from the time recording of the cutting force obtained numerically.

It is worth to correlate f_{force} with the mean shear band spacing L_s characterized in the previous section. In that purpose, we introduce another relevant definition of the segmentation frequency, $f_{segment}$, derived from the time period $(\Delta t)_{segment} = L_1/V_{chip}$ necessary to form a chip segment of length $L_1 = L_s/\cos\phi_s$, see Fig. 3b. Thus, we have

$$f_{segment} = 1/(\Delta t)_{segment} = V_{chip}/L_1 \tag{20}$$

The average chip velocity, V_{chip}, is determined from volume conservation

$$V_{chip} = V(t_1/\bar{t}_2) \tag{21}$$

In the idealized view of Fig. 3b, the inclination of shear bands is characterized by the angle ϕ_s which is related to the mean chip thickness $\bar{t}_2$ by Eq. (7). Then, Eq. (20) can be written as

$$f_{segment} = \frac{Vt_1}{L_s\bar{t}_2}\cos(\arctan(t_1/\bar{t}_2)) \tag{22}$$

f_{force} and $f_{segment}$ are displayed in Fig. 11a in terms of the cutting speed for $t_1 = 100\ \mu m$. It is seen that force oscillations (f_{force}) are well correlated to chip segmentation ($f_{segment}$). In Fig. 11a the frequency of segmentation appears to be proportional to

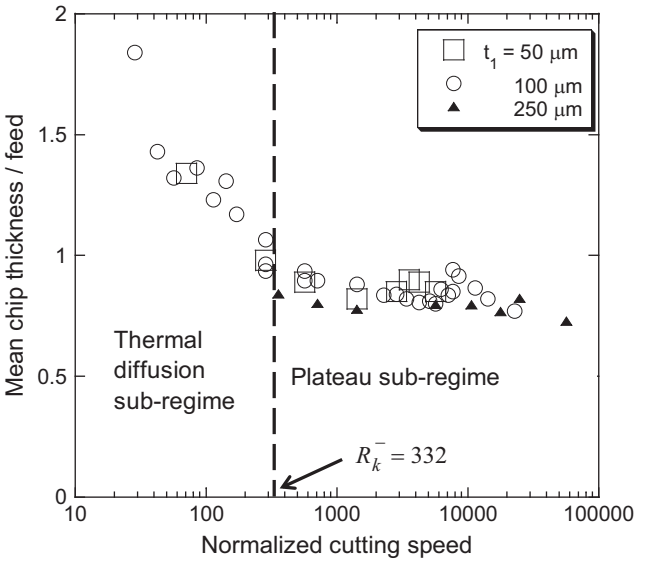

Fig. 10. Normalized mean chip thickness $\bar{t}_2/t_1$ with respect to the normalized cutting speed $R_k = \rho C_p t_1 V/k$ in semi-log scaling. The transition to the plateau sub-regime (where $\bar{t}_2/t_1$ is nearly constant) occurs at the value $R_k^- = 332$, as in Fig. 5b. In the plateau sub-regime, the process is adiabatic at the scale of the mean chip thickness $\bar{t}_2$.

the cutting speed. This result agrees with Eq. (22) if we recall that L_s and $\bar{t}_2/t_1$ are nearly insensitive to the cutting speed V in the plateau sub-regime $V^- < V < V^+$, see Figs. 5b, c and 10. Cutting speeds larger than $V^+ = 270$ ms^{-1} (supercritical regime) are not displayed in Fig. 11a. For these velocities, the shear band spacing is significantly reduced and consequently an abrupt increase of the segmentation frequency would be seen.

Another outcome of Eq. (22) is that $f_{segment}$ should be inversely proportional to the feed t_1 on the plateau sub-regime, since L_s is proportional to the feed in this regime while $\bar{t}_2/t_1$ is independent of t_1. The results shown in Fig. 11b confirm this dependence. In Fig. 11c, $f_{segment}$ is rescaled by the multiplicative factor $t_1(\mu m)/100$, so that all results are merging on the curve associated to the feed $t_1 = 100 \mu m$.

In Fig. 12 $f_{segment}$ is displayed in terms of the cutting speed V in a log–log scaling. Results of simulations at the feed $t_1 = 100\ \mu m$ are compared to experimental data of Molinari et al. (2002) (with $t_1 = 120\ \mu m$) and Cotterell and Byrne (2008) (with $t_1 = 100\ \mu m$). In the experiments of Molinari et al. (2002) cutting speeds from 0.01 m/s to 40 m/s were obtained by using a ballistic set-up for $V > 10\ m/s$ and a hydraulic machine for lower cutting speeds. The frequency of segmentation was derived from the time period defined as the ratio of the cutting time by the number of shear bands counted in the recovered chip. The correlation between theoretical prediction and experimental measurements appears to be quite satisfactory for the range of cutting speeds $V > 1.5\ m/s$ for which the theory predicts the existence of thermal shear bands (it is recalled that $V_{onset} = 1.5\ m/s$ is the theoretical threshold above which chip serration is activated when $t_1 = 100\ \mu m$, see Fig. 4). The results follow a slope equal to one for $V > 1.5\ m/s$, indicating that the frequency of segmentation is proportional to the cutting speed as predicted in Fig. 11.

However, experimental results indicate that the slope is different from 1 for $V < 1.5\ m/s$. For these low velocities, chip flow instabilities are experimentally triggered but these instabilities cannot be predicted by the present theory. Here, it should be recalled that thermal softening is the sole mechanism of shear banding introduced in the modeling. Thermal softening is certainly a prevalent mechanism of chip serration at large cutting speeds, but other weakening mechanisms may predominate at low cutting speeds (dynamic recrystallisation, material damage by micro-voiding etc.). Dynamic recrystallisation seems to be an important softening mechanism in Ti–6Al–4V (Rittel et al., 2008). The existence at low velocities of weakening mechanisms, different from thermal softening, may be the reason for the change of slope associated to experimental data for $V < 1.5\ m/s$ observed in Fig. 12. Therefore, the theoretical framework should be augmented by additional softening mechanisms to describe chip segmentation at low cutting speeds. In the present work the focus is made on thermal effects which allow for describing chip segmentation for large enough cutting speeds ($V > 1.5\ m/s$ for $t_1 = 100\ \mu m$).

3.8. Intensity of segmentation and cutting force

The segmentation index S_i defined by Eq. (9) characterizes the intensity of chip serration. For fragmented chip (discontinuous chip) S_i is defined by considering the chip morphology prior to fracture. We note that $S_i = 0$ when the chip is uniform and that S_i increases with the intensity of strain localization (characterized as the ratio of the average strain

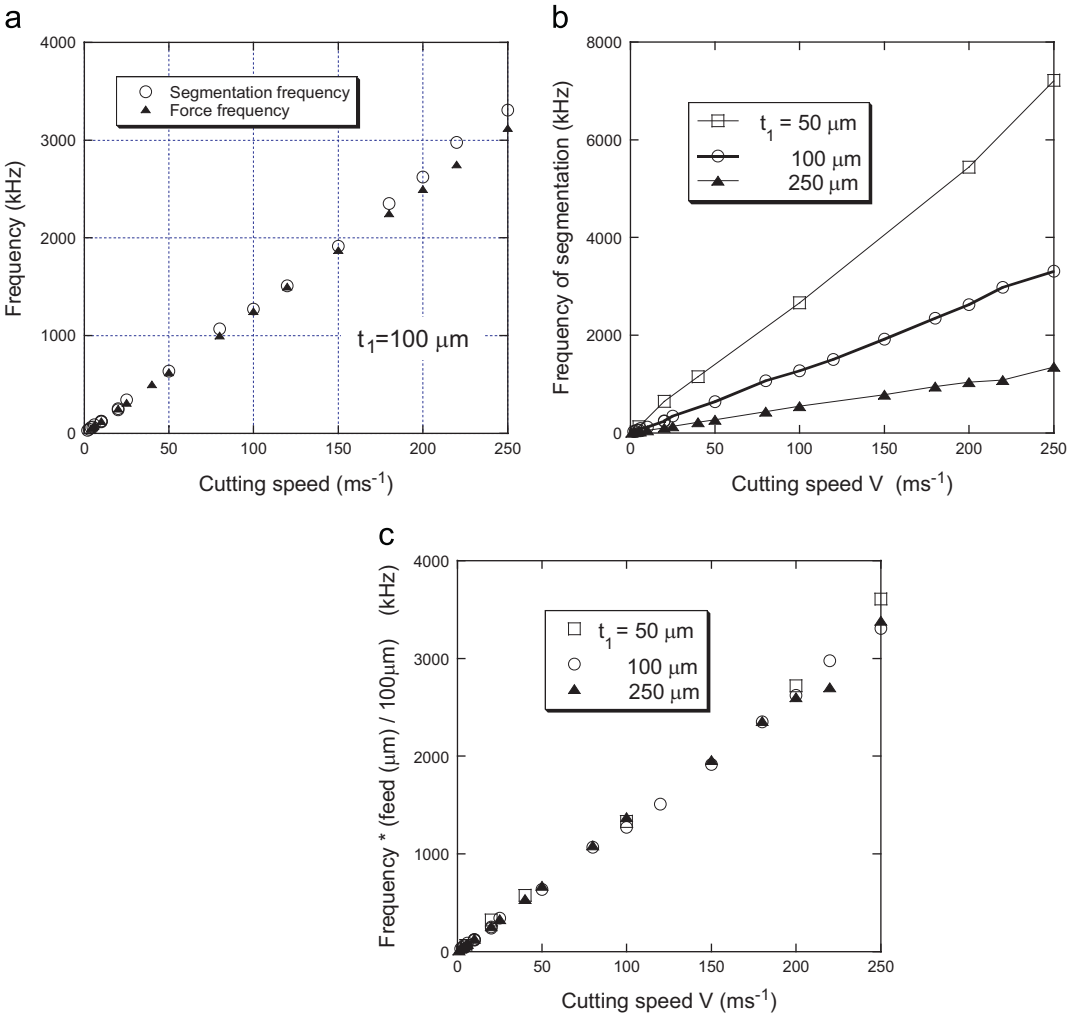

Fig. 11. (a) Frequency of segmentation $f_{segment}$ in terms of the cutting speed V for $t_1 = 100\ \mu m$. $f_{segment}$ is proportional to the cutting speed. $f_{segment}$ appears to be well correlated to the frequency f_{force} of force oscillations. (b) Effect of the feed t_1 on $f_{segment}$. (c) $f_{segment}$ is rescaled by the multiplicative factor $t_1(\mu m)/100$. Since all results are merging on the line associated to the feed $t_1 = 100\ \mu m$, it follows that $f_{segment}$ is inversely proportional to the feed t_1.

in a band by the average strain between two bands) (Atlati et al., 2011). Higher intensity of strain localization (i.e. higher S_i) is associated to at least one of the following factors:

(F1) larger shear band spacing and
(F2) smaller shear band width.

The dependence of S_i and of the specific cutting force F_x/t_1 with respect to the normalized cutting speed $R_k = \rho C_p t_1 V/k$ is illustrated in Fig. 13a and b for several values of the feed. F_x denotes the time average of the component of the cutting force in the direction of the cutting speed. It is recalled that forces per unit cutting width are considered.

In Fig. 13a, a rather good correlation is found between the trends for S_i provided by simulation results and experimental data from Gente and Hoffmeister (2001), Bäker et al. (2002) and Chen et al. (2011). Experimental conditions are given in Table 3. S_i was obtained by our own measurements from the chip morphologies displayed in these papers. The comparison with experimental results will be further examined in Section 3.10.

There is a striking similarity between evolutions of S_i and F_x/t_1. It is seen that S_i increases first, then passes by a maximum and finally decays to zero. The variation of F_x/t_1 goes in the opposite way. For low velocities (thermal diffusion sub-regime), both evolutions are ruled by the normalized velocity $R_k = \rho C_p t_1 V/k$, the results for various feeds being clustered along a well defined ascending branch for S_i and descending branch for F_x/t_1. On the contrary, the results are dispersed at large values of R_k. This provides a confirmation that (i) for low values of the quantity Vt_1 (small R_k), chip serration is essentially governed by heat transfer effects as already observed in Section 3.3 and (ii) other physical aspects are involved at high cutting speeds as indicated by the dispersion of results at large values of R_k.

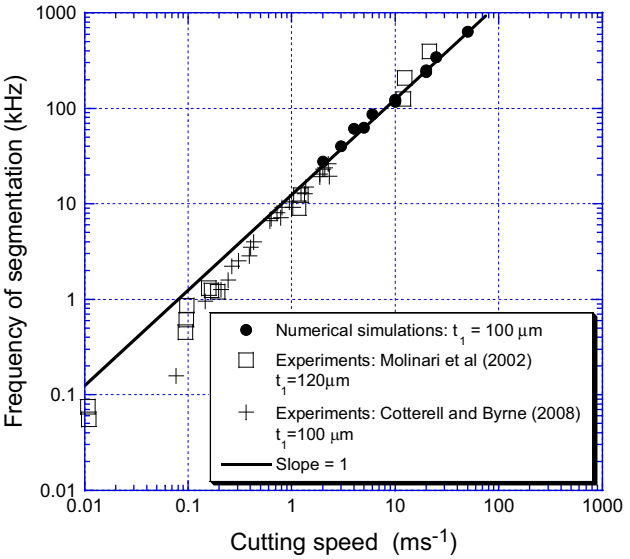

Fig. 12. Frequency of segmentation $f_{segment}$ vs cutting speed V. FEM simulations for $t_1 = 100\ \mu m$ (filled circles) are displayed against experimental data of Molinari et al. (2002) obtained for $t_1 = 120\ \mu m$, and those of Cotterell and Byrne (2008) for $t_1 = 100\ \mu m$. The slope equal to 1 obtained for $V > 1.5\ m/s$ in the present log–log diagram indicates that $f_{segment}$ is proportional to V. The good correlation observed between simulations and experiments in this range of cutting speeds suggests that thermal softening and adiabatic shear banding is likely to be the cause of chip segmentation for $V > 1.5\ m/s$. For lower cutting speeds ($V < 1.5\ m/s$), chip serration is observed in the experiments but not in the simulations. Therefore, other mechanisms of chip serration than thermal softening are expected to be activated for $V < 1.5\ m/s$.

In Fig. 13a the increasing of S_i starts at about $R_k^{segm} = 40$, which is in agreement with the analysis of the onset of flow instability developed in Section 3.2. The end of the rapid growth of S_i occurs at about the critical value $R_k^- = 332$ that was found to characterize the transition from the thermal diffusion sub-regime to the plateau regime of shear band spacing, see Section 3.3 and Fig. 5b.

Similarly, the normalized cutting force F_x/t_1 starts to decrease at about $R_k^{segm} = 40$, Fig. 13b, and the force drops rapidly up to the end of the thermal diffusion sub-regime which is characterized by $R_k^- = 332$.

Increasing the cutting speed promotes adiabatic conditions that in turn stimulate thermal softening and flow instability. This leads to higher strain concentration within shear bands and to the increasing of S_i. The opposite trend observed for F_x/t_1 makes sense since a larger value of S_i is associated to stronger shear localization, higher temperature within shear bands and higher tool–chip interface temperature that together induce a decreasing of the cutting force by thermal softening.

It is well known that plastic flow localization is slowed down by inertia at high strain rates. This is a general feature that is true for dynamic necking (Fressengeas and Molinari, 1994; Mercier and Molinari, 2003; Zhou et al., 2006a) and adiabatic shear banding. For shear localization this was demonstrated with finite difference simulations and perturbation analysis by Molinari (1985), see also Wright and Ockendon (1996) and Molinari (1997). Thus, inertia effects that are significant at high cutting speeds can contribute to the decreasing of S_i by slowing down the process of strain concentration within bands (stabilizing effect due to local inertia forces that impede the movement of particles subject to high accelerations within the shear zone).

To corroborate the idea that the process is significantly influenced by inertia at high cutting speeds, results for S_i and F_x/t_1 are displayed in Fig. 14 in terms of the cutting speed. It is seen that, at high cutting speeds, results are grouped along a well defined descending branch for S_i , Fig. 14a, and a well defined ascending branch for F_x/t_1, Fig. 14b. This is a proof that for large values of V , chip serration and specific cutting force are not depending upon the feed t_1 and are solely controlled by velocity i.e. by inertia (represented by the inertial number R_I, Eq. (4)). It is noticeable that inertia effects begin to be significant when approaching the cutting velocity of $100\ ms^{-1}$. It is also worth noting that the sharp drop of the segmentation index S_i occurs at about $V^+ = 270\ ms^{-1}$ characterizing the transition to the supercritical regime of shear banding.

By contrast, results in Fig. 14a and b are dispersed at low velocities, while they were grouped along well defined curves in Fig. 13a and b where results were displayed in terms of R_k.

So far, the calculations were performed for fixed values of the nominal mesh size ($\delta = 1.5\ \mu m$ for $t_1 = 50\ \mu m$; $\delta = 3\ \mu m$ for $t_1 = 100\ \mu m$ and $\delta = 5\ \mu m$ for $t_1 = 250\ \mu m$). This is sufficient as long as trends related to the evolution of S_i versus cutting speed are the sole interest. However, for quantitative comparison with experimental results, the convergence analysis of Appendix A should be used. This aspect will be further discussed in Section 3.10.

The evolution of the specific cutting force F_x/t_1 in terms of cutting speed displayed in Fig. 14b can be compared to experimental data of Molinari et al. (2002), Hoffmeister et al. (1999) and Larbi (1990). The minimum of the force was found

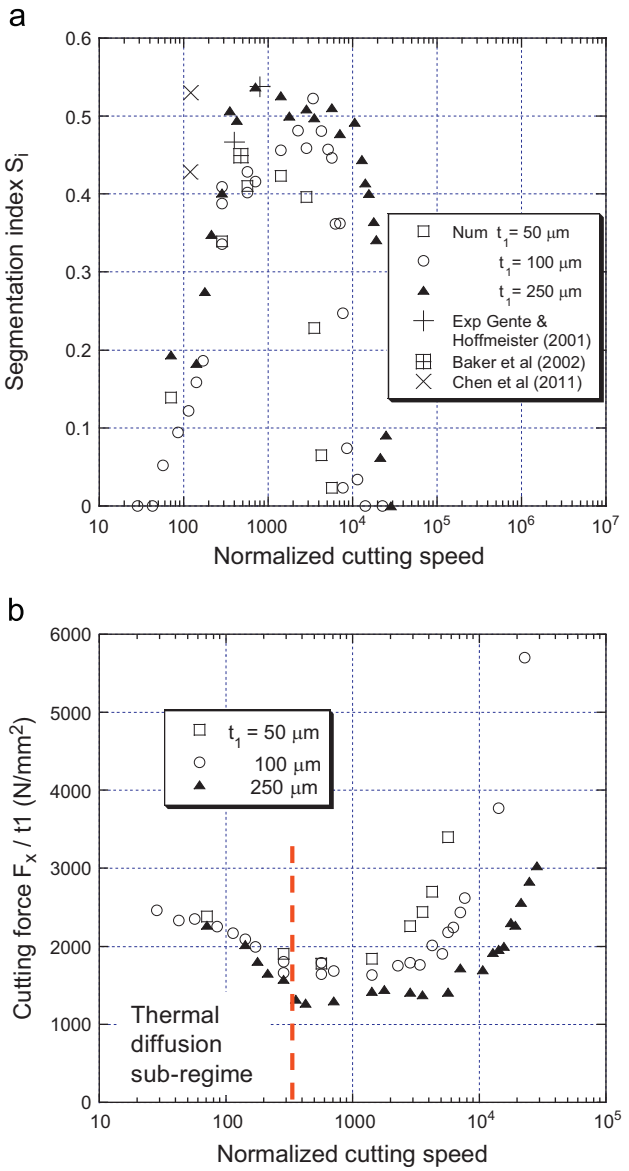

Fig. 13. (a) Segmentation index S_i and (b) specific cutting force F_x/t_1 vs the normalized cutting speed $R_k = \rho C_p t_1 V/k$. Simulation results are shown for various values of the feed t_1. Results for S_i are well correlated to experimental data of Gente and Hoffmeister (2001), Bäker et al. (2002) and Chen et al. (2008) which are reported in Table 3. It is also seen that at small values of R_k the data are well gathered along master curves (ascending branch of S_i and the descending branch of F_x/t_1). On the contrary the results are dispersed for large values of R_k. This shows that for small values of the cutting speed, the process of chip formation and of shear banding is controlled by thermal effects (thermal softening and heat diffusion).

to be 950 N/mm^2 for Larbi (1990), 1200 N/mm^2 for Molinari et al. (2002) (feed of 120 μm) and 1900 N/mm^2 for Hoffmeister et al. (1999). Variations between these results may be attributed in part to the difference of thermo-mechanical treatment and microstructure between the materials tested. In our simulations the minimum of F_c/t_1 depends on the feed and varies between 1300 and 1800 N/mm^2. However, with a finer mesh size providing better accuracy, the force level would be decreased by 10–20%, see figure 21 of Appendix A. But, the opposite variation is obtained (increasing of the force) by considering the effect of the tool edge radius. Altogether, the force evaluated in the simulations is comparable to experimental data. The characterization of the cutting speed at which the force is minimum is also instructive. In the ballistic experiments of Molinari et al. (2002) the minimum was found at about 70 m/s. This value is in agreement with the simulation results displayed in Fig. 14b.

The increasing of F_x/t_1 at high cutting speed is due to inertia effects. The effect of inertia on the cutting force can be evaluated analytically in the case of uniform chip (no chip serration). This condition is approached when the cutting speed is increased since the segmentation index drops when entering into the supercritical regime. It is known that F_x can be

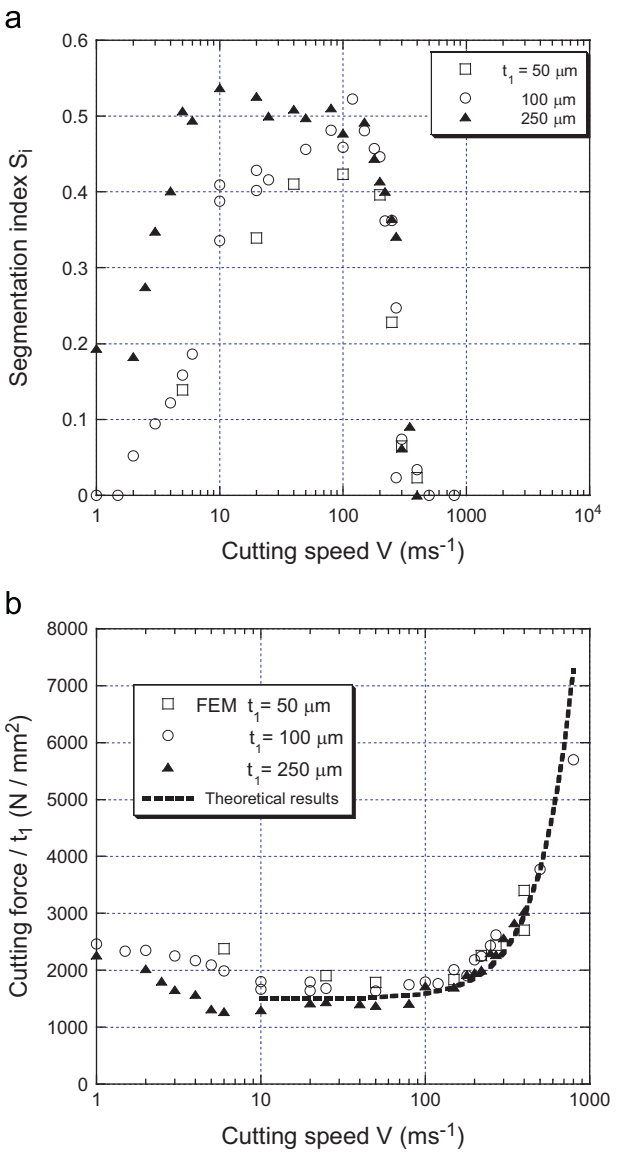

Fig. 14. (a) Segmentation index S_i and (b) specific cutting force F_x/t_1 vs cutting speed V. Simulation results are shown for the same values of the feed as in Fig. 13. It is seen that for large values of V the data are well gathered along master curves (descending branch of S_i and the ascending branch of F_x/t_1). On the contrary the results are dispersed for low values of V. These features can be explained by the growing importance of inertia effects at high cutting speeds while thermal diffusion becomes less effective. From the dimensional analysis, it appears that, at large cutting speeds, S_i and F_x/t_1 are controlled by the dimensionless inertial parameter $R_I = \rho V^2/A$ that does not depend upon feed. The prominence of inertia for $V > 70\ m/s^{-1}$ is further illustrated for the specific cutting force. The dashed line is based on theoretical results, Eqs. (23) and (25), that account for inertia effects in chip formation. These results are in perfect agreement with FEM data.

decomposed into a quasistatic term and an inertial contribution (Arndt, 1973; Recht, 1984; Dudzinski and Molinari, 1997):

$$F_x = F_x^{static} + F_x^{dyn} \tag{23}$$

F_x^{static}/t_1 depends on the shear flow stress of the work-material and on the shear angle ϕ (orientation of the primary shear zone). For $\alpha = 0$, we have

$$\frac{F_x^{dyn}}{t_1} = \rho V^2 \frac{\cos(\lambda^{ap})}{\cos\phi\cos(\phi+\lambda^{ap})} \tag{24}$$

ϕ is close to 45° at cutting speeds larger than 10 m/s. λ^{ap} is the apparent friction angle characterizing the overall frictional response of the tool–chip interface. For cutting speeds larger than 10 m/s the overall friction coefficient is small, see Molinari et al. (2011). Therefore, a reasonable estimate of F_x^{dyn}/t_1 is obtained by taking $\cos(\lambda^{ap}) \approx 1$ and $\cos(\phi+\lambda^{ap}) \approx \cos(\phi) = \sqrt{2}/2$.

It follows that

$$\frac{F_x^{dyn}}{t_1} = 2\rho V^2 \tag{25}$$

Following Eqs. (23) and (25) we have

$$F_x/t_1 = F_x^{static}/t_1 + 2\rho V^2 \tag{26}$$

This theoretical result is reported in Fig. 14b with the value $F_x^{stat}/t_1 = 1500\ N/\mathrm{mm}^2$ calibrated at the level of the cutting force at intermediate cutting speeds. It is clearly seen that the inertia effect predicted by Eq. (25) matches quite well the trend given by the Finite Element simulations (parabolic growth as V^2). From the quasistatic theory of metal cutting (Merchant, 1945) F_x^{stat}/t_1 is scaled by the yield stress of the work material, i.e. by the parameter A in the Johnson–Cook law (1). Therefore, according to Eq. (26), the relative contribution of inertia to the cutting force is scaled by the inertial number $R_I = \rho V^2/A$. These considerations illustrate the role of the inertial number in the evolution of the cutting force at high velocities.

Finally, the global evolution of the cutting force can be viewed as follows. For relatively low cutting speeds, the cutting force decreases by increasing the cutting speed. This is due to thermal effects that soften the overall frictional response at the tool-chip interface in the range of cutting speeds $V < 10$ m/s (as discussed by Molinari et al., 2011) and to chip serration by adiabatic shearing. At high cutting speed inertia dominates the evolution of the cutting force. Inertia effects reduce the intensity of chip serration (decreasing of the segmentation index S_i). The decreasing of S_i contributes in turn to the growth of the cutting force (a variation of S_i produces the opposite trend on the cutting force). However, at large cutting speeds the increasing of the cutting force is mainly governed by the overall change of momentum in the chip flow which contributes to an increasing of the cutting force scaled by ρV^2, Eq. (26). The segmentation index S_i is rapidly tending to zero and therefore does not contribute anymore to the evolution of the cutting force at very high cutting speeds.

3.9. Characterization of the transition to the supercritical regime

The questions addressed in this section are the following. What is the physical origin of the sharp transition to the supercritical regime of shear band spacing ? Can the transition velocity V^+ be characterized theoretically?

It was previously pointed out that inertia effects play a crucial role in the transition from subcritical to supercritical regime of shear banding. This was attested by the results shown in Figs. 5c and 14a. At a certain value of the cutting speed V^+ (independent from the feed t_1) a sharp drop of the shear band spacing and of the segmentation index S_i are observed. It was noticed in Section 3.8 that inertia plays a stabilizing role that slows down plastic flow localization within shear bands when strain rates are augmented. However, there exists another effect that is also related to inertia and that can strongly influence the decay of S_i and the transition to the supercritical regime.

Let us recall that shear bands are nucleated sequentially at the tool tip. After being nucleated, a band propagates towards the free surface of the chip. We denote by C_S the (time average) propagation speed of a shear band. Regarding the chip segmentation problem, two important characteristic times can be defined: (i) the time , $t_{propagation}$, necessary for a shear band to propagate through the chip thickness and reach the free surface and (ii) the time, $t_{convection}$, for a shear band to be convected away from the chip formation region by material flow . A shear band has no enough time to reach the free surface of the chip if $t_{propagation} > t_{convection}$. As a matter of fact, in this case the shear band is arrested at the time $t = t_{convection}$ at which it leaves the primary shear zone (considering that $t = 0$ is the nucleation time of the band). Thus, chip serrations are much attenuated when $t_{propagation} > t_{convection}$. Such a case is illustrated in Fig. 15 showing the chip morphology and strain contours for $V = 350\ \mathrm{ms}^{-1}$ and $t_1 = 100\ \mu m$. The chip thickness appears as almost uniform. A family of shear bands is clearly seen but none of them reach the free surface of the chip.

According to the present analysis, the transition to vanishing serrations occurs for $t_{propagation} = t_{convection}$. This criterion can be quantified. The orientation of shear bands at high cutting speeds is about 45° with respect to the cutting speed direction (Fig. 15). Thus, we have $t_{propagation} \approx (\bar{t}_2\sqrt{2})/C_S$, with $\bar{t}_2\sqrt{2}$ being the mean distance to be covered by a shear band to attain the free surface. On the other hand, we have $t_{convection} \approx w_{PSZ}\sqrt{2}/V_{chip}$ where w_{PSZ} is the thickness of the primary shear zone (chip formation region). From volume conservation it follows that $\bar{t}_2 V_{chip} = t_1 V$. By estimating that $w_{PSZ} \approx a t_1$ (with a of the order of 0.2–0.4), it turns out that $t_{convection} \approx a\bar{t}_2\sqrt{2}/V$. Thus the criterion $t_{propagation} > t_{convection}$ corresponding to the extinction of chip serration takes the form

$$V/a > C_S. \tag{27}$$

As later commented, the shear band speed C_S is function of the cutting speed V. Thus, according to the criterion (27), the cutting speed V^+ beyond which the segmentation index drops abruptly (onset of the supercritical regime of shear band spacing) is given by the intersection of the straight line V/a with the curve $C_S(V)$, i.e. by the relationship:

$$V^+ = a\, C_S(V^+) \tag{28}$$

The shear band speed C_S is displayed in Fig. 16a in terms of the cutting speed V for the feed $t_1 = 100\ \mu m$. The speed C_S was estimated by following the propagation of strain isoclines with time, see Bonnet-Lebouvier et al. (2002). For $V < V_{segm}$ there

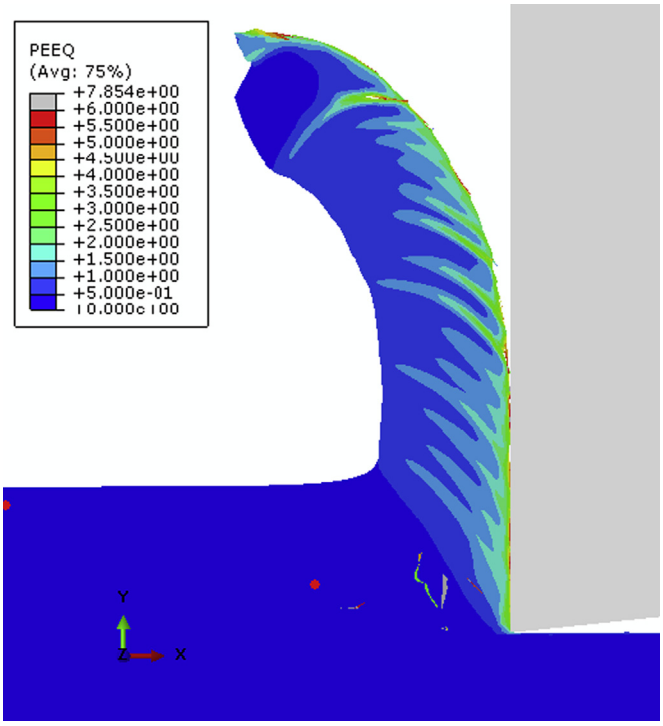

Fig. 15. Chip morphology and strain isoclines for $V = 350$ ms^{-1} and $t_1 = 100\ \mu m$. A family of shear bands is clearly seen within the chip. However, at this high level of the cutting speed, the shear bands have no enough time to reach the free surface of the chip. This is an effect of chip flow convection that pushes shear bands away from the chip formation region before they can be fully developed.

is no shear banding. For $V > V_{segm}$, it is seen in Fig. 16a that C_S increases almost linearly with V for small cutting speeds. However, at large cutting speed ($V > 100$ ms^{-1}) C_S saturates to the asymptotic value 700 ms^{-1}.

Similar trends were observed by Zhou et al. (1996a, 1996b) when considering a pre-notched plate (made up of C300 steel) subject to the impact of a projectile. Their experimental results revealed that, beyond a certain critical impact velocity, an adiabatic shear band is generated at the notch tip and propagates with an average speed C_S that increases with the impact velocity. These trends were confirmed by their numerical simulations. The analysis of the onset and propagation of adiabatic shear bands in the configuration of thin tubes subject to rapid torsion (experiments of Marchand and Duffy (1988) on torsional Kolsky bars) was addressed by Batra and Zhang (1994) and Bonnet-Lebouvier et al. (2002). The latter authors developed a theoretical modeling providing the same trends as those observed by Zhou et al. (1996a, 1996b) for impact loading of pre-notched plates. It was observed by Bonnet-Lebouvier et al. (2002) that C_S is tending asymptotically to a limit value $C_S^{\lim}$ at high cutting speeds.

The configuration of orthogonal cutting experiments bears some similarities with the above mentioned works since the material is subject in all cases to intense shear loading. Thus, similar trends are obtained for the dependence of C_S with respect to the loading velocity V, the latter being the impact velocity for Zhou et al. (1996a, 1996b), the shear velocity applied at the boundaries of a layer for Bonnet-Lebouvier et al. (2002) and the cutting speed in the present work. This similarity can be illustrated by comparing the results of Fig. 16a to those reported in figure 5 of Bonnet-Lebouvier et al. (2002) for a CRS1018 steel. Although the materials are distinct (Ti-6Al-4V in the present work) and the experimental configuration are different, the limit $C_S^{\lim}$ is reached at comparable values of the applied velocity (about $V = 150$ ms^{-1} in both cases). The value $C_S^{\lim}$ is also comparable (about 700 ms^{-1} for cutting of Ti-6Al-4V as compared to 800 ms^{-1} for the case of CRS1018 steel analyzed by Bonnet-Lebouvier et al. (2002)). Such a coincidence in quantitative values is fortuitous, but the trend towards an asymptotic limiting value is in any case robust.

From Fig. 16b it is seen that for $a > 0.2$ the intersection of the straight line V/a with the curve $C_S(V)$ (Eq. (28)) occurs on the plateau associated to $C_S^{\lim} = 700$ ms^{-1}. Thus, we have $V^+ = 700a$ (ms^{-1}). For $0.2 \le a \le 0.4$ (corresponding to typical values of w_{PSZ} which are usually considered to be between 20% and 40% of the uncut chip thickness t_1) we obtain 140 ms^{-1} $\le V^+ \le$280 ms^{-1}. The result $V^+ = 270$ ms^{-1} given by the present numerical modeling falls within this range. This value of V^+ corresponds to $a = 0.368$ as illustrated in Fig. 16b.

For $V > V^+$, shear bands have no time to reach the free surface of the chip. Consequently, the chip is just mildly wavy and becomes in fact uniform when the cutting speed is still augmented. In addition, for $V > V^+$, the numerical simulations reveal that several bands are growing together within the chip formation region and mutual interactions take place between these bands. Consequently, the shear band spacing decreases with the cutting speed (Fig. 7). The possibility for several bands to grow together is related to the fact that shear localization cannot fully develop within a given band when $t_{propagation} > t_{convection}$. Consequently, the unloading process in the chip formation region is weak and a growing band cannot

impede the nucleation of the subsequent band. The opposite situation prevails in the subcritical regime $(V < V^+)$ where just a single well developed shear band is growing at a time in the chip formation region.

It can be checked that the saturation value, $C_S^{\lim} \approx 700\ \mathrm{ms}^{-1}$, is weakly sensitive to the feed t_1. Thus, V^+ characterized as in Fig. 16b appears to be also insensitive to t_1, in agreement with the results found in Section 3.4.

It was demonstrated by Bonnet-Lebouvier et al. (2002) that the limit value $C_S^{\lim}$ at high loading velocities is related to inertia effects that control the propagation of the band via the elastic release rate, the speed of elastic shear waves and the variation of kinetic energy of material elements through the process zone at the tip of the band. Thus, it can be concluded that inertia effects are responsible of the transition to the supercritical regime of shear band spacing through several aspects. Firstly, shear flow localization is slowed down by inertia at very high cutting speeds and consequently the chip segmentation index is reduced as previously noticed. Secondly, the relationship found between V^+ and $C_S^{\lim}$ indicates that the transition to the supercritical regime of shear banding is also ruled by inertia through the asymptotic limit $C_S^{\lim}$.

3.10. Effect of damage

In our modeling, fracture of a material element occurs when the accumulated plastic strain reaches the critical value ε_{crit}. In the calculations, elements are deleted when this critical condition is reached. Therefore cracks can propagate along shear

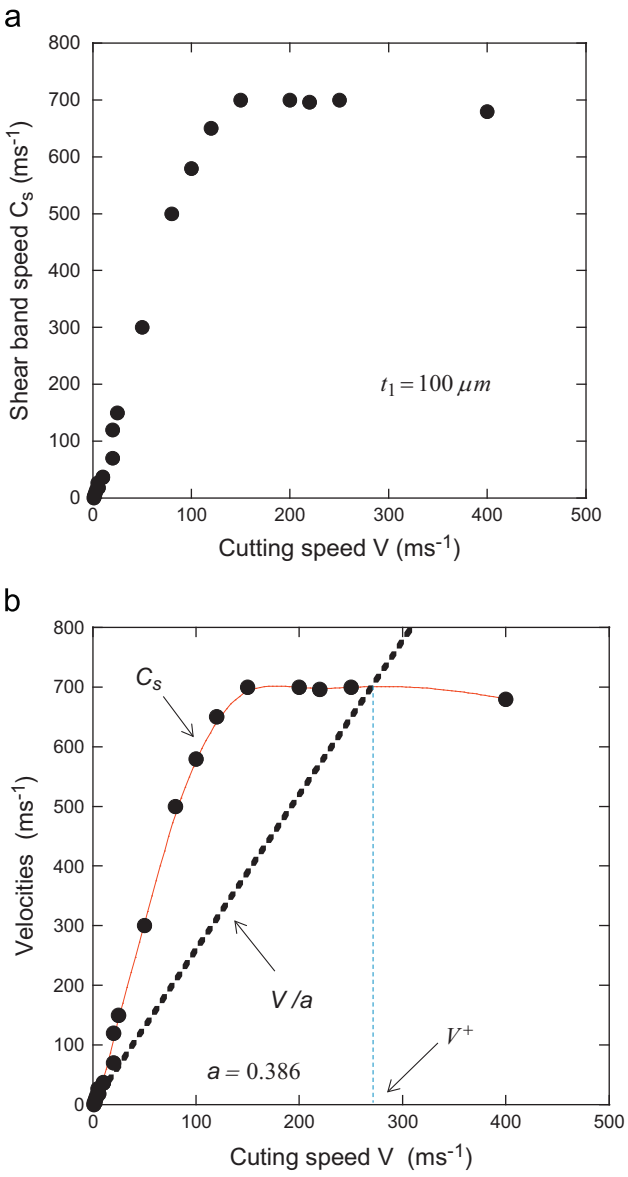

Fig. 16. (a) Propagation speed C_s (time average) of a shear band versus cutting speed. We note that the asymptotic value 700 ms^{-1} is reached at high cutting speeds. (b) Characterization of the transition cutting speed V^+ according to criterion Eq. (28).

bands where plastic strain is localized. In a certain range of cutting speeds, the chip can be completely fragmented in small segments by crack propagation along shear bands. It is recalled that for a completely fragmented chip, S_i characterizes the chip morphology prior to chip fracture.

The effect of ε_{crit} on S_i is analyzed in Fig. 17a for the feed $t_1 = 100\,\mu m$. With the low value of the damage parameter $\varepsilon_{crit} = 3$ damage and crack propagation are favoured. Consequently, the segmentation index is augmented as compared to the case $\varepsilon_{crit} = 8$. However, the onset of chip flow instability at $V_{segm} \approx 1.5$ ms^{-1} is not affected by ε_{crit} (see Fig. 17a) since the damage parameter ε_{crit} is only operant at large strains. It is also observed that the transition to the supercritical regime at $V^+ = 270$ ms^{-1} is not affected by ε_{crit} probably because the threshold values considered here ($\varepsilon_{crit} = 3$ and 8) are too high for material failure to affect $C_S^{\lim}$.

S_i was compared to experimental results in Fig. 13a for a restricted range of cutting speeds. Characterizations of chip morphologies were recently obtained by Sutter and List (2013) by performing the same experiments on lathe and ballistic set-up as Molinari et al. (2002) allowing to explore cutting speeds up to $70 ms^{-1}$. Their measurements of the segmentation

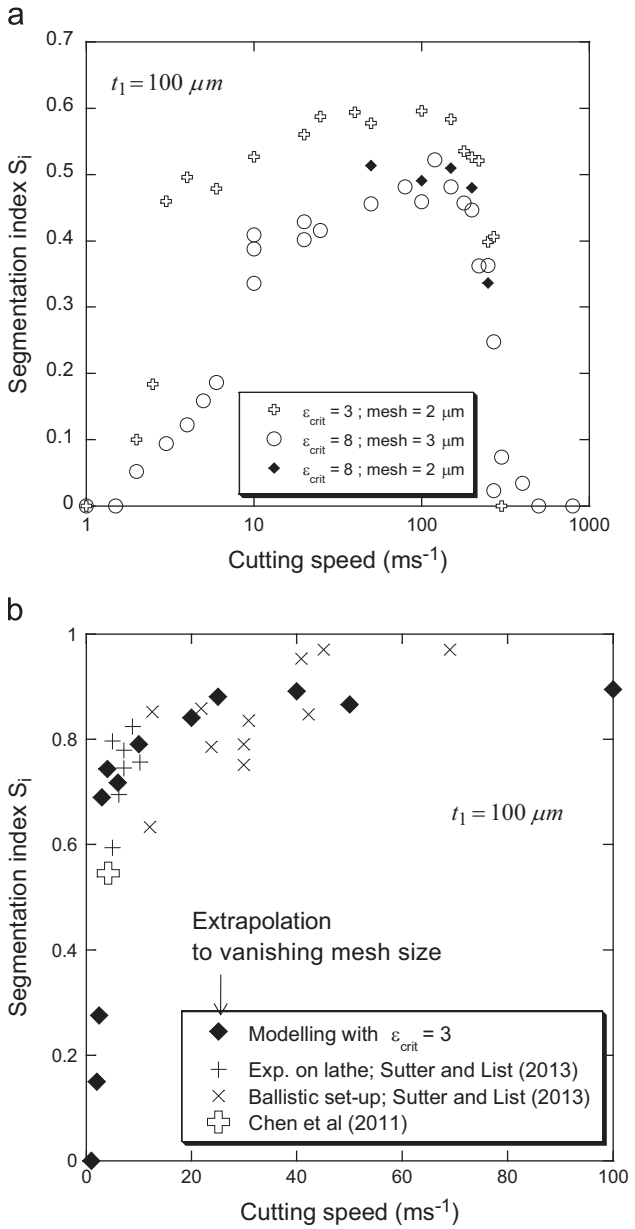

Fig. 17. (a) Effect of the damage parameter ε_{crit} on the segmentation index S_i for $t_1 = 100\,\mu m$. A lower value of ε_{crit} favours crack propagation along shear bands and is therefore conducive to higher values of S_i. It is seen that the onset of chip flow instability at $V_{segm} \approx 1.5$ ms^{-1} and the transition to the supercritical regime at $V^+ = 270$ ms^{-1} are not affected by ε_{crit}. (b) Simulation results of S_i obtained with $\varepsilon_{crit} = 3$ are compared against experimental data up to the cutting speed $V = 70$ ms^{-1}.

index S_i in terms of cutting speed is reported in Fig. 17b for the feed $t_1 = 100\ \mu m$ together with a result from Chen et al. (2011) at the cutting speed $V = 4.2\ \mathrm{ms}^{-1}$.

For a quantitative comparison between experimental data and theory, two aspects of the modeling will be discussed. Firstly, it is recalled that ε_{crit} is the sole adjustable parameter in the model. This parameter allows for calibrating the amount of damage within shear bands and has consequently an influence on the segmentation index. The results of Fig. 17a show that the level of S_i can be significantly increased by considering lower values of the damage parameter ε_{crit}.

Secondly, for this quantitative comparison, the convergence analysis developed in Appendix A is considered (see Fig. 20). According to this analysis , values of S_i extrapolated at vanishing mesh size should be about 50% higher than those obtained with the mesh size of 3 μm used so far for $t_1 = 100\ \mu m$. The extrapolation at vanishing mesh size is made in Fig. 17b showing the evolution of S_i in terms of the cutting speed. The value $\varepsilon_{crit} = 3$ considered in Fig. 17b provides a quite good correlation between experiments and modeling.

It should be noted that results on the shear band spacing are weakly sensitive to the value of ε_{crit} in the range explored $3 \le \varepsilon_{crit} \le 12$. This point is checked in Appendix A for $V < V^+$, Fig. 19.

More interesting than quantitative agreement is the correspondence between experimental trends and those predicted by the modeling: a rapid increasing of S_i at small cutting speeds followed by a saturation at high cutting speeds. These trends are conserved for all values of ε_{crit} considered here. Indeed, it is worth noticing that all phenomena discussed in this work are essentially preserved whatever is the value of ε_{crit} in the range $3 \le \varepsilon_{crit} \le 12$. For instance, V_{segm} and V^+ appeared in Fig. 17a to be insensitive to ε_{crit}.

4. Summary and discussion

Thermal softening and the damage criterion ε_{crit} are the sole mechanisms of material weakening considered in the present modeling of chip serration. Thermal softening becomes operative at high enough cutting speeds when the process is tending to adiabatic conditions. Fragmentation occurs at large plastic strains and is governed by the limit strain ε_{crit}.

The main findings are summarized in Fig. 18.

- The onset of chip flow instability and chip serration occurs at the cutting speed $V_{segm} = kR_k^{segm}/\rho C_p t_1$ with $R_k^{segm} = 40$.
- Shear band spacing (and chip serration) is governed by two distinct regimes (subcritical and supercritical regimes). For Ti–6Al–4V, the transition between these regimes occurs at the cutting speed $V^+ = 270\ \mathrm{ms}^{-1}$. For $V < V^+$ (subcritical regime), each shear band propagates through the entire chip thickness. Shear bands are formed sequentially and do not interact with each other. For $V > V^+$ (supercritical regime), shear bands are incompletely formed (they do not reach the free surface of the chip, see Fig. 15) and they interact with each other. The transition between subcritical and supercritical regimes manifests itself by a sudden drop of shear band spacing and chip serration.
- Within the subcritical regime $(V < V^+)$ several sub-regimes can be distinguished for the mean shear band spacing L_S

thermal-diffusion sub-regime: At low cutting speeds L_S/t_1 (average shear band spacing divided by feed) is controlled by thermal diffusion through the dimensionless cutting speed (thermal number) $R_k = \rho C_p t_1 V/k$. Below the critical value $R_k^{segm} = 40$ no thermal shear bands are observed in the simulations and the chip is continuous. The onset of shear banding occurs at the value $R_k^{segm} = 40$. L_S/t_1 increases with R_k for $R_k < R_k^- = 332$. The transition to the plateau regime occurs at the cutting speed $V^- = kR_k^-/\rho C_p t_1$. Thus L_S increases with V for $V_{onset} < V < V^-$.

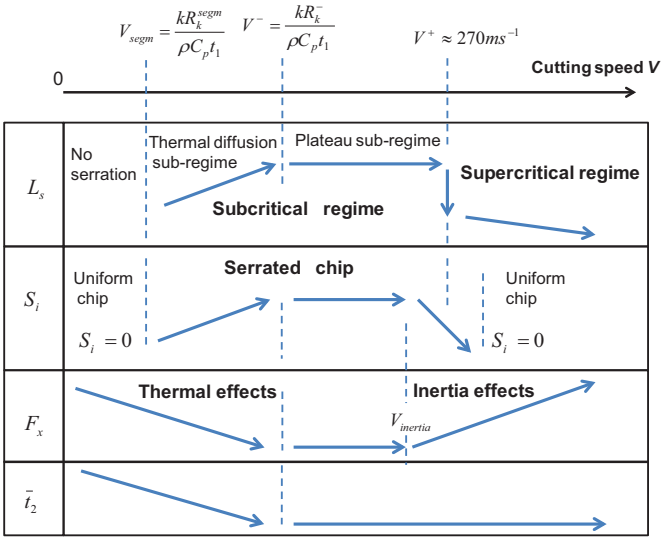

Fig. 18. Summary of results concerning the different regimes of chip serration and the evolution of cutting force and chip mean thickness.

plateau sub-regime: Beyond the critical value $R_k^- = 332$, the normalized shear band spacing L_S/t_1 becomes nearly independent of cutting speed and feed. The plateau sub-regime corresponds to adiabatic conditions at the scale of the shear band spacing. Inertia effects are negligible in the thermal-diffusion sub-regime and in most of the plateau sub-regime.

inertial sub-regime: For high cutting velocities , $V > 70$ ms^{-1}, inertia effects become operative. The time average cutting force increases in proportion to $\rho\, V^2$. The transition towards the supercritical regime happens at the cutting speed $V^+ = 270$ ms^{-1} with a sudden drop of the shear band spacing, Fig. 5c.

• The supercritical regime occurs when shear bands have no enough time to propagate from the tool tip to the free surface of the chip. This feature is a manifestation of inertia, as the propagation of a shear band is controlled by inertia effects at high velocities. A sudden drop of the segmentation index is observed when shear bands do not reach the free surface of the chip. Chip serration is also reduced by the stabilizing effects of inertia that slow down plastic flow localization. Thus, inertia can be viewed as the dominant factor governing the supercritical regime (by saturating the propagation speed of shear bands and slowing down the shear localization process within bands). The value of the transition velocity $V^+ = 270$ ms^{-1} could be estimated with a criterion based on characteristic propagation and convection times. This criterion illustrates the interference between adiabatic shear banding and convective flow.

• The shear band spacing is drastically reduced in the supercritical regime. Several shear bands are growing together within the chip formation region and interactions take place between these bands. Trends concerning the dependence of the shear band spacing with respect to the cutting speed can be predicted with the linearized perturbation approach or the momentum diffusion theory.

• It has been also shown that the segmentation index and the shear band spacing follow similar variations in terms of the cutting speed, while the cutting force shows an opposite trend. These trends are summarized in Fig. 18 together with those related to the mean chip thickness.

• It should be recalled that the model contains some simplifications. The modeling of damage refers to a critical value, ε_{crit}, of the accumulated plastic strain for which a material element loses completely its stress carrying capacity. This criterion was successfully used to model fragmentation for high strain rate processes, see for instance the works of Rusinek and Zaera (2007) and Rodriguez-Martinez et al. (2013) on fragmentation of dynamically expanding rings. More sophisticated damage laws may be used that involve the effect of loading conditions and of pressure to describe material failure by crack propagation.

• The effect of the damage parameter ε_{crit} on chip serration was investigated. The segmentation index S_i is significantly increased in the plateau regime when ε_{crit} is reduced from 8 to 3 and the cutting force is decreased. However, the shear band spacing and consequently the segmentation frequency are weakly sensitive to ε_{crit} in the range explored ($3 < \varepsilon_{crit} < 12$). Also, the onset of shear banding, the transition to the supercritical regime and in general all the trends observed in this work are similar whatever is the value of ε_{crit}.

• The present model of chip serration has been validated experimentally for a large range of cutting speeds and feeds. However, extrapolations to very high cutting speeds should be considered with some caution. In particular, the

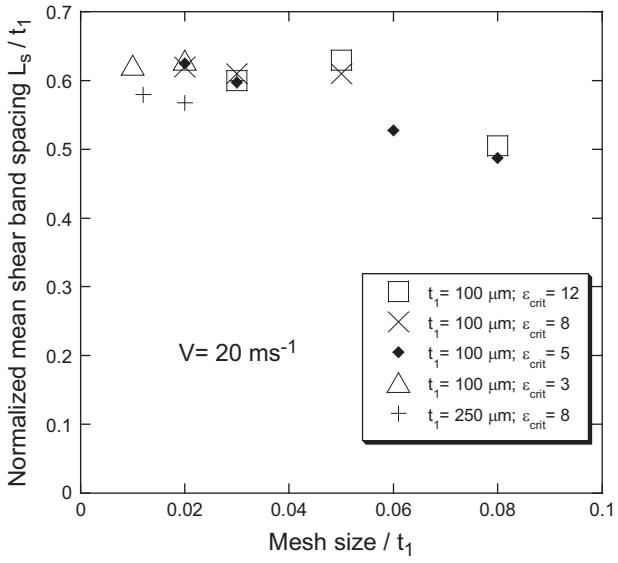

Fig. 19. Simulation results showing the normalized mean shear band spacing L_s/t_1 in terms of the normalized mesh size δ/t_1 for the cutting speed, $V = 20$ ms^{-1}, and for various values of the feed t_1 and of the damage parameter ε_{crit}. It is seen that convergence is achieved for $\delta/t_1 < 0.05$ and that ε_{crit} does not affect much the results.

disappearance of chip serration for $V > V^{+} = 270\ \mathrm{ms}^{-1}$ observed in the present modeling means that chip segmentation is hardly feasible by the sole effect of adiabatic shear banding and material failure based on the concept of limit strain ε_{crit}. Nevertheless, another mechanism of material failure may predominate in these extreme loading conditions. Experimental data are needed to improve the modeling for extremely high velocities. In any case, it appears useful to have preliminary results with a simplified approach that could be confronted against experimental results to push forward the theory.

5. Conclusions

Shear banding in orthogonal cutting was theoretically investigated by Finite Element calculations combined with analytical considerations. The proposed approach provides a general framework explaining how chip formation is affected by adiabatic shear banding. The effects of feed (uncut chip thickness) and cutting speed were systematically analysed and rationalized. A classification of the different regimes of shear banding has been proposed. The underlying physical aspects associated to these regimes have been elucidated and characterized in terms of scaling laws involving dimensionless parameters related to heat conduction and inertia effects.

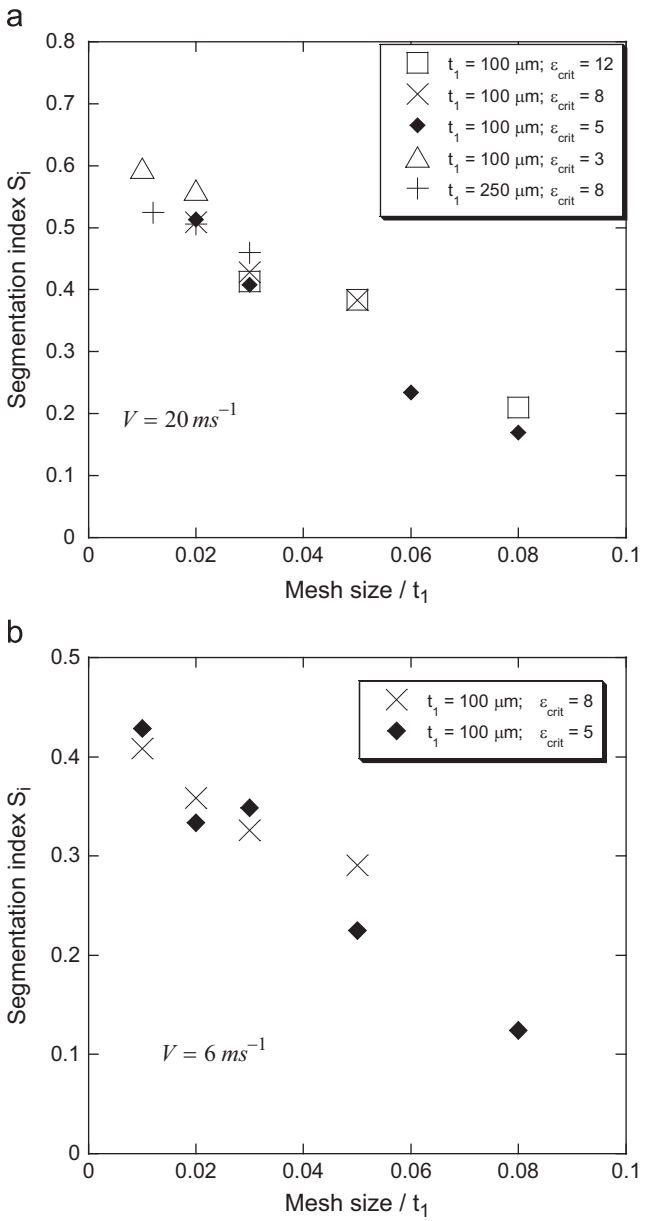

Fig. 20. Segmentation index S_i in terms of the normalized mesh size δ/t_1 for various values of the feed t_1 and of the damage parameter ε_{crit}: (a) cutting speed $V = 20\ \mathrm{ms}^{-1}$ and (b) $V = 6\ \mathrm{ms}^{-1}$.

The results were compared against experimental data for Ti–6Al–4V alloy in a wide range of cutting speeds and feeds, but the methodology can be applied to other materials and the theoretical results presented have a general character.

The fundamental knowledge developed in this work is thought to be useful not only for the understanding of metal cutting processes but also, by analogy, to similar problems where convective flow is also interfering with adiabatic shear banding as in impact mechanics and perforation processes. In that perspective, cutting speeds higher than those usually encountered in machining operations have been explored.

Acknowledgments

A.M. wishes to acknowledge the support of Carlos III University with a Catedra de Excelencia funded by Banco Santander. This work was also supported by the French State through the program "Investment in the future" operated by the National Research Agency (ANR) and referenced by LabEx DAMAS.

Appendix A. Sensitivity analysis with respect to mesh size and mesh orientation

The dependence of L_s with respect to the mesh size δ is illustrated in Fig. 19 for the cutting speed $V=20$ m/s , the feeds $t_1=100$ μm and $t_1=250$ μm and several values of the deletion parameter ε_{crit}. It is seen that L_s becomes independent of the mesh size when δ/t_1 is smaller than 0.05. The level of the damage parameter ε_{crit} has a moderate influence on results. When varying the cutting speed, it can be checked that convergence is achieved in a similar way as for $V=20$ m/s.

Fig. 20a shows the evolution of the segmentation index S_i (defined by Eq. (9)) in terms of δ/t_1 for various values of the feed t_1 and of the damage parameter ε_{crit}. S_i is a decreasing and affine function of δ/t_1. The segmentation index increases significantly from the value 0.15 at $\delta/t_1=0.08$ to about 0.7 when the mesh size decreases to zero. In Fig. 20b the cutting speed has a smaller value, $V=6$ m/s. The segmentation index is reduced, the same affine dependence of S_i with respect to δ/t_1 is conserved. From these results, it appears that S_i can be estimated by extrapolating the results at vanishing mesh size. Thus, to analyze the segmentation index, one needs to work with finer mesh size than for the analysis of the shear band spacing. As we are mostly interested by analysing trends, calculations are made for the fixed value $\delta/t_1=0.03$ to save computational time (except for the feed $t_1=250$ μm for which we took $\delta/t_1=0.02$).

However, when the modeling is compared against experimental results, accurate quantitative results can be obtained by extrapolating the values of S_i to vanishing mesh size, see Fig. 17b.

Fig. 21 shows the dependence of the time average specific cutting force, F_x/t_1 with respect to the normalized mesh-size δ/t_1. It is seen that F_x/t_1 increases with the mesh size. Here again, the value of the specific cutting force can be obtained by extrapolating the results at vanishing mesh size.

To summarize, the shear band spacing can be accurately defined by using mesh-sizes such that $\delta/t_1 \leq 0.05$. The segmentation index and the cutting force can be obtained by extrapolating results at vanishing mesh size, taking advantage of the affine trends illustrated in Figs. 20–21. In any case, the above results show that to compare results obtained at different feeds, it is better using mesh sizes that are proportional to the feed (same values of δ/t_1).

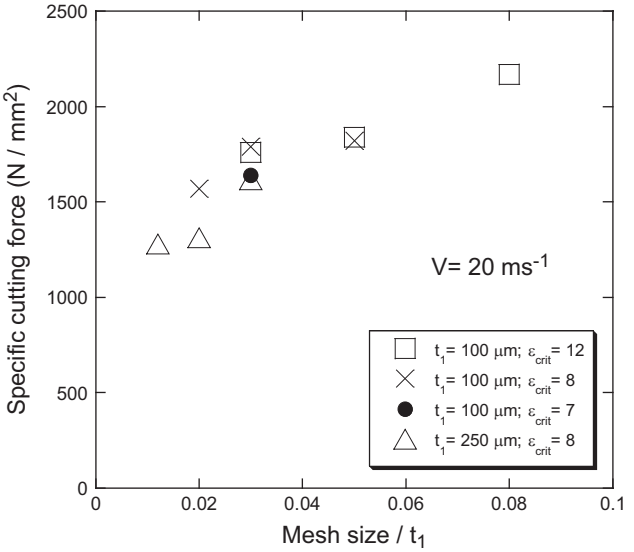

Fig. 21. Specific cutting force, F_x/t_1, in terms of the normalized mesh-size δ/t_1.

Table 4
Cutting force F_x in terms of the mesh orientation θ. Simulations are carried out for the feed $t_1 = 100\ \mu m$, the deletion parameter $\varepsilon_{crit} = 8$ and mesh size $\delta = 5\ \mu m$. The minimum of F_x is obtained at $\theta = 45^\circ$.

V=6 m/s			
θ (deg)	40	45	50
F_x (N/mm)	228	211	223
V=20 m/s			
F_x (N/mm)	193	183	205

Simulations have been conducted by considering the mesh orientation, $\theta = 45^\circ$ in zone A. This value was chosen since it corresponds to the optimum orientation for which the time average, F_x, of the cutting force is minimum, i.e. for which the rate of cutting work, $F_x V$, is minimized. This is in line with usual optimization procedures used in numerical methods.

For illustration, we have reported in Table 4 the values of the cutting force F_x for two cutting speeds and several mesh orientations. It is seen that F_x is minimum for $\theta = 45^\circ$. This value was used in all simulations.

References

Abaqus Manual, 2003. Version 6.4, Hibbit. Karlsson & Sorenson Inc., Providence, USA.
Arndt, G., 1973. Ultra high speed machining: a review and an analysis of cutting forces. Proc. Inst. Mech. Eng. 187, 625–634.
Atlati, S., Haddag, B., Nouari, M., Zenasni, M., 2011. Analysis of a new segmentation intensity ratio "SIR" to characterize the chip segmentation process in machining ductile metals. Int. J. Mach. Tools Manuf. 51, 687–700.
Bai, Y.L., 1982. Thermo-plastic instability in simple shear. J. Mech. Phys. Solids 30, 195–207.
Bai, Y., Dodd, B., 1992. Adiabatic Shear localization. Pergamon, Oxford.
Bäker, M., Rösler, J., Siemers, C., 2002. A finite element model of high speed metal cutting with adiabatic shearing. Comput. Struct. 80, 495–513.
Batra, R.C., Zhang, X.T., 1994. On the propagation of a shear-band in a steel tube. J. Eng. Mater. Technol.-Trans. ASME 116, 155–161.
Batra, R.C., Ravinsankar, M.V.S., 2000. Three-dimensional simulation of the Kalthoff experiment. Int. J. Fract. 105, 161–186.
Bayoumi, A.E., Xie, J.Q., 1995. Some metallurgical aspects of chip formation in cutting Ti–6 wt% Al–4 wt% V alloy. Mater. Sci. Eng. A 190, 173–180.
Bonnet-Lebouvier, A.S., Molinari, A., Lipinski, P., 2002. Analysis of the dynamic propagation of adiabatic shear bands. Int. J. Solids Sruct. 39, 4249–4269.
Burns, T.J., Davies, M.A., 2002. On repeated adiabatic shear band formation during high-speed machining. Int. J. Plasticity 18, 487–506.
Calamaz, M., Coupard, D., Girot, F., 2008. A new material model for 2D numerical simulation of serrated chip formation when machining titanium alloy Ti–6Al–4V. Int. J. Mach. Tools Manuf. 48, 275–288.
Chen, G., Ren, C., Yang, X., Jin, X., Guo, T., 2011. Finite element simulation of high-speed machining of titanium alloy (Ti–6Al–4V) based on ductile failure model. Int. J. Adv. Manuf. Technol. 56, 1027–1038.
Childs, T.H.C., (in press). Adiabatic shearing in metal machining. CIRP Encyclopedia of Production Engineering, Springer-Verlag, in press.
Clifton, R.J., 1980. Adiabatic Shear Banding. Chapter 8 in Material Response to Ultra-high Loading Rates, NMAB-356. National Academy of Sciences, Washington, DC.
Cotterell, M., Byrne, G., 2008. Dynamics of chip formation during orthogonal cutting of titanium alloy Ti–6Al–4V. CIRP Ann.—Manuf. Technol. 57, 93–96.
Cox, T.B., Low, J.R., 1974. An investigation of the plastic fracture of AISI 4340 and 18 Nickel-200 grade Maraging steels. Metall. Trans. 5, 1457–1470.
Davies, M.A., Burns, T.J., Evans, C.J., 1997. On the dynamics of chip formation in machining hard metals. Ann. CIRP 46, 25–30.
Dodd, B., Atkins, A.G., 1983. Flow localization in shear deformation of void-containing and void-free solids. Acta Metall. 31, 9–15.
Dudzinski, D., Molinari, A., 1997. A modeling of cutting for viscoplastic materials. Int. J. Mech. Sci. 39, 369–389.
Fressengeas, C., Molinari, A., 1994. Fragmentation of rapidly stretching sheets. Eur. J. Mech. A/Solids 13, 251–268.
Gente, A., Hoffmeister, H.W., 2001. Chip formation in machining Ti6Al4V at extremely cutting speed. Ann. CIRP 50, 49–52.
Grady, D.E., 1992. Properties of an adiabatic shear band process zone. J. Mech. Phys. Solids 40, 1197–1215.
Grady, D.E., Kipp, M.E., 1987. The growth of unstable thermoplastic shear with application to steady-wave shock compression in solids. J. Mech. Phys. Solids 35, 95–118.
Hoffmeister, H.W., Gente, A., Weber, T.H., 1999. Chip formation at titanium alloys under cutting speed of up to 100 m/s. In: Schulz, H., Molinari, A., Dudzinski, D. (Eds.), Proceedings of the 2nd International Conference on High Speed Machining. PTW Darmstadt University, pp. 21–28.
Hortig, C., Svendsen, B., 2007. Simulation of chip formation during high-speed cutting. J. Mater. Process. Technol. 186, 66–76.
Johnson, G.R., Cook, W.H., 1983. A constitutive model and data for metals subjected to large strains, high strain rate and temperature. In: Proceedings of the 7th International Symposium of Ballistics, The Hague, pp. 541–547.
Klepaczko, J.R., 1994. An experimental technique for shear testing at high and very high strain rates, the case of mild steel. Int. J. Impact Eng. 15, 25–39.
Komanduri, R., von Turkovich, B.F., 1981. New observations on the mechanism of chip formation when machining titanium alloys. Wear 69, 179–188.
Larbi, S., 1990. Contribution à l'Etude de l'Usinage à Grandes Vitesses de Matériaux Métalliques par Simulation sur un Banc d'Essai à Base de Barres de Hopkinson. Th. Doctorat, Université de Nantes, France.
Lee, W.-S., Lin, C.-F., 1998. High-temperature deformation behaviour of Ti6Al4V alloy evaluated by high strain-rate compression tests. J. Mater. Process. Technol. 75, 127–136.
Lovinger, Z., Rikanati, A., Rosenberg, Z., Rittel, D., 2011. Electro-magnetic collapse of thick-walled cylinders to investigate spontaneous shear localization. Int. J. Impact Eng. 38, 918–929.
Marchand, A., Duffy, J., 1988. An experimental study of the formation process of adiabatic shear bands in a structural steel. J. Mech. Phys. Solids 36, 251–283.
Merchant, E., 1945. Mechanics of the metal cutting process—I. Orthogonal cutting. J. Appl. Phys. 16, 267–275.
Mercier, S., Molinari, A., 1998. Steady-state shear band propagation under dynamic conditions. J. Mech. Phys. Solids 46, 1463–1495.
Mercier, S., Molinari, A., 2003. Predictions of bifurcation and instabilities during dynamic extension. Int. J. Solids Struct. 40, 1995–2016.
Meyers, M.A., Meyer, L.W., Vecchio, K.S., Andrade, U., 1991. High strain, high strain-rate deformation of copper. J. Phys. III 1 (C3), 11–17.
Meyers, M.A., Kuriyama, S., 1986. Numerical modeling of the propagation of an adiabatic shear band. Metall. Trans. 17 A, 433–450.
Molinari, A., 1985. Thermo-viscoplastic instability in simple shear. J. Theor. Appl. Mech. 4, 659–684.
Molinari, A., 1997. Collective behavior and spacing of adiabatic shear bands. J. Mech. Phys. Solids 45, 1551–1575.
Molinari, A., Cheriguene, R., Miguélez, H., 2011. Numerical and analytical modeling of orthogonal cutting: the link between local variables and global contact characteristics. Int. J. Mech. Sci. 53, 183–206.

Molinari, A., Cheriguene, R., Miguelez, H., 2012. Contact variables and thermal effects at the tool–chip interface in orthogonal cutting. Int. J. Solids Struct. 49, 3774–3796.
Molinari, A., Clifton, R., 1983. Localisation de la déformation viscoplastique en cisaillement simple. C. R. Acad. Sci. 296 (II), 1–4.
Molinari, A., Clifton, R.J., 1987. Analytical characterization of shear localization in thermoviscoplastic materials. ASME J. Appl. Mech. 54, 806–812.
Molinari, A., Musquar, C., Sutter, G., 2002. Adiabatic shear banding in high speed machining of Ti–6Al–4V: experiments and modeling. Int. J. Plasticity 18, 443–459.
Moufki, A., Devillez, A., Dudzinski, D., Molinari, A., 2004. Thermomechanical modeling of oblique cutting and experimental validation. Int. J. Mach. Tools Manuf. 44, 971–989.
Nesterenko, V.F., Meyers, M.A., Chen, H.C., LaSavia, J.C., 1994. Controlled high-rate localized shear in porous reactive media. Appl. Phys. Lett. 65, 3069–3071.
Obikawa, T., Usui, E., 1996. Computational machining of titanium alloy—finite element modeling and a few results. J. Manuf. Sci. Eng.—Trans. ASME 118, 208–215.
Recht, R.F., 1964. Catastrophic thermoplastic shear. Trans. ASME J. Appl. Mech. 31, 189–193.
Recht, R.F., 1984. A dynamic analysis of high speed machining. In: Komanduri, R., et al. (Eds.), High Speed Machining. ASME, New York, pp. 83–93.
Rittel, D., Landau, P., Venkert, A., 2008. Dynamic recrystallization as a potential cause of adiabatic shear failure. Phys. Rev. Lett.. (Article number 165501).
Rittel, D., Lee, S., Ravichandran, G., 2002. A shear-compression specimen for large strain testing. Exp. Mech. 9, 58–64.
Rodriguez-Martinez, J.A., Vadillo, G., Fernandez-Saez, J., Molinari, A., 2013. Identification of the critical wavelength responsible for the fragmentation of ductile rings expanding at very high strain rates. J. Mech. Phys. Solids 61, 1357–1376.
Rogers, H.C., 1979. Adiabatic plastic deformation. Ann. Rev. Mater. Sci. 9, 283–311.
Rusinek, A., Zaera, R., 2007. Finite element simulation of steel ring fragmentation under radial expansion. Int. J. Impact Eng. 34, 799–822.
Soldani, X., Muñoz-Sánchez, A., Miguélez, H., Molinari, A., 2010. Numerical modeling of segmentation phenomenon in orthogonal cutting. In: Proceedings of the 2nd CIRP International Conference Process Machine Interactions, Vancouver, Canada, pp. 10–11.
Subbiah, S., Melkote, S.N., 2008. Effect of finite edge radius on ductile fracture ahead of the cutting tool edge in micro-cutting of Al2024-T3. Mater. Sci. Eng. A 474, 283–300.
Sun, S., Brandt, M., Dargusch, M.S., 2009. Characteristics of cutting forces and chip formation in machining of titanium alloys. Int. J. Mach. Tools Manuf. 49, 561–568.
Sutter, G., List, G., 2013. Very high speed cutting of Ti–6Al–4V titanium alloy–change in morphology and mechanism of chip formation. Int. J. Mach. Tools Manuf. 66, 37–43.
Sutter, G., Molinari, A., List, G., Bi, X., 2012. Chip flow and scaling laws in high speed metal cutting. J. Manuf. Sci. Eng., 134. Article Number 021005.
Tresca, H., 1878. On further application of the flow of solids. Proc. Inst. Mech. Eng. 30, 301–345.
Wright, T.W., 1990. Approximate analysis for the formation of adiabatic shear bands. J. Mech. Phys. Solids 38, 515–530.
Wright, T.W., 1994. Towards a defect invariant basis for susceptibility to adiabatic shear bands. Mech. Mater. 17, 215–222.
Wright, T.W., 2002. The Physics and Mathematics of Adiabatic Shear Bands. Cambridge Univ. Press, Cambridge.
Wright, T.W., Batra, R.C., 1985. The initiation and growth of adiabatic shear bands. Int. J. Plasticity 1, 202–212.
Wright, T.W., Ockendon, H., 1996. A scaling law for the effect of inertia on the formation of adiabatic shear bands. Int. J. Plasticity 12, 927–934.
Wright, T.W., Walter, J.W., 1987. On stress collapse in adiabatic shear bands. J. Mech. Phys. Solids 35, 701–720.
Ye, G.G., Xue, S.F., Jiang, M.Q., Tong, X.H., Dai, L.H., 2013. Modeling periodic shear band evolution during high speed machining Ti–6Al–4V alloy. Int. J. Plasticity 40, 39–55.
Zener, C., Hollomon, J.H., 1944. Effect of strain rate upon plastic flow. J. Appl. Phys. 15, 22–32.
Zhou, F., Molinari, J.F., Ramesh, K.T., 2006a. An elastic-visco-plastic analysis of ductile expanding ring. Int. J. Impact Eng. 33, 880–891.
Zhou, F., Wright, T.W., Ramesh, K.T., 2006b. The formation of multiple adiabatic shear bands. J. Mech. Phys. Solids 54, 1376–1400.
Zhou, M., Rosakis, A.J., Ravichandran, G., 1996a. Dynamically propagating shear band in impact-loaded prenotched plates: I—experimental investigations of temperature signatures and propagation speed. J. Mech. Phys. Solids 44, 981–1006.
Zhou, M., Ravichandran, G., Rosakis, A.J., 1996b. Dynamically propagating shear band in impact-loaded prenotched plates: II—numerical simulations. J. Mech. Phys. Solids, 44; 1007–1032.